Physics of the Earth and Planetary Interiors 252 (2016) 1–22

Contents lists available at ScienceDirect

Physics of the Earth and Planetary Interiors

journal homepage: www.elsevier.com/locate/pepi

P and S wave tomography of Japan subduction zone from joint inversions of local and teleseismic travel times and surface-wave data

Xin Liu *, Dapeng Zhao *

Department of Geophysics, Tohoku University, Sendai 980-8578, Japan

ARTICLE INFO

Article history:
Received 19 August 2015
Received in revised form 8 January 2016
Accepted 10 January 2016
Available online 16 January 2016

Keywords:
Seismic tomography
Joint inversion
Body wave
Rayleigh wave
Japan subduction zone
Earthquakes

ABSTRACT

We determined P and S wave velocity tomography of the Japan subduction zone down to a depth of 700 km by conducting joint inversions of a large number of high-quality arrival-time data of local earthquakes and teleseismic events which are newly collected for this study. We also determined 2-D phase-velocity images of fundamental mode Rayleigh waves at periods of 20–150 s beneath Japan and the surrounding oceanic regions using amplitude and phase data of teleseismic Rayleigh waves. A detailed 3-D S-wave tomography of the study region is obtained by jointly inverting S-wave arrival times of local and teleseismic events and the Rayleigh-wave phase-velocity data. Our inversion results reveal the subducting Pacific and Philippine Sea slabs clearly as dipping high-velocity zones from a 1-D starting velocity model. Prominent low-velocity (low-V) anomalies are revealed in the mantle wedge above the slabs and in the mantle below the Pacific slab. The distinct velocity contrasts between the subducting slabs and the surrounding mantle reflect significant lateral variations in temperature as well as water content and/or the degree of partial melting. The low-V anomalies in the mantle wedge are attributed to slab dehydration and corner flows in the mantle wedge. A sheet-like low-V zone is revealed under the Pacific slab beneath NE Japan, which may reflect hot upwelling from the deeper mantle and subduction of a plume-fed asthenosphere as well. Our present results indicate that joint inversions of different seismic data are very effective and important for obtaining robust tomographic images of the crust and mantle.

1. Introduction

The Japan subduction zone belongs to the Western Pacific trench–arc–backarc system, where the Pacific plate, the Eurasian plate, the Philippine Sea (PHS) plate and the Okhotsk plate strongly interact with each other (Fig. 1). The Pacific plate is subducting beneath the Okhotsk plate, the PHS plate, and the Eurasian plate along the Kuril–Japan–Izu-Bonin trench, whereas the PHS plate is subducting beneath the Eurasian plate along the Nankai trough and the Ryukyu trench. The strong interactions among these plates have resulted in many active arc volcanoes and large earthquakes, such as the 2011 Tohoku-oki earthquake (*Mw* 9.0) sequence (Fig. 1).

So far many researchers have studied the three-dimensional (3-D) velocity structure of the Japan subduction zone using abundant data recorded by the dense seismic networks installed on the Japan Islands (see a recent review by Zhao (2015)). Most of these studies focused on the velocity structure down to ~200 km depth, including the crust, mantle wedge, and the upper portion of the subducting Pacific slab. These previous studies have greatly improved our understanding of arc magmatism, forearc mantle serpentinization, seismotectonics and subduction dynamics of this region (e.g. Hasegawa et al. (2013), Liu and Zhao (2014, 2015), Zhao et al. (2016)). However, only a few studies investigated the fine deep structure of the Japan subduction zone, besides the large-scale regional and global tomography (e.g. Friederich (2003), Gorbatov and Kennett (2003), Zhao (2004), Huang and Zhao (2006), Koulakov (2011), Obayashi et al. (2013), Chen et al. (2015b), Wei et al. (2012, 2015)). Zhao et al. (1994) determined a 3-D P-wave velocity (Vp) model of the Japan subduction zone down to 500 km depth by conducting a joint inversion of travel-time data of local earthquakes and teleseismic events. They used 4211 travel-time residuals of 100 teleseismic events recorded by seismic stations in NE Japan. Later, Abdelwahed and Zhao (2007) adopted the same approach to obtain an improved 3-D Vp model down to 700 km depth beneath Japan. They used 34,148 relative residuals of 333 teleseismic events recorded by seismic stations on the Japan Islands. The teleseismic data used in these previous studies, however, were not sufficient in both quantity and quality, because

* Tel.: +81 22 225 1950; fax: +81 22 264 3292.
E-mail addresses: liuxin@ouc.edu.cn (X. Liu), dapeng.zhao.d2@tohoku.ac.jp (D. Zhao).

http://dx.doi.org/10.1016/j.pepi.2016.01.002
0031-9201/

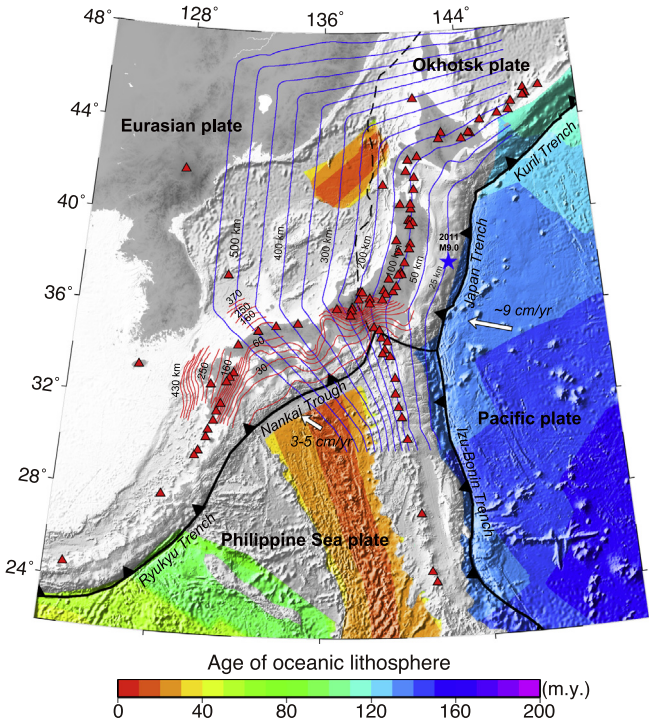

Fig. 1. Tectonic settings of the study region (after Liu et al. (2013a)). The red triangles denote the active and Quaternary volcanoes. The solid sawtooth lines and the black dashed line denote the plate boundaries. The blue and red lines denote the depth contours to the upper boundary of the subducting Pacific and Philippine Sea slabs, respectively, which are constructed based on several previous studies (e.g. Zhao et al. (1994, 1997a, 2012), Nakajima et al. (2009), Hasegawa et al. (2013), Huang et al. (2013), Asamori and Zhao (2015)). (For interpretation of the references to color in this figure legend, the reader is referred to the web version of this article.)

the data were mainly recorded by the old and sparse seismic network, J-Array (Zhao et al., 1994; Abdelwahed and Zhao, 2007). Using all the previous teleseismic data recorded by the J-array and ~11,500 data from 27 teleseismic events recorded by the High-Sensitivity Seismic Network (Hi-net) that covers the Japan Islands densely and uniformly (Okada et al., 2004), Zhao et al. (2012) determined a high-resolution Vp tomography of the crust and mantle down to 700 km depth beneath the Japan Islands. Recently, Asamori and Zhao (2015) presented a detailed shear-wave velocity (Vs) tomography of the Japan subduction zone down to 700 km depth using 34,122 S-wave arrival times of 51 teleseismic events recorded by the Hi-net. They also obtained an updated 3-D Vp model down to 700 depth using 5,878 P-wave arrival times they picked up from the Hi-net waveforms of 8 teleseismic events and ~45,400 P-wave arrivals from 360 teleseismic events collected by the previous studies (Zhao et al., 1994, 2012; Abdelwahed and Zhao, 2007). These tomographic results show similar features of the deep structure beneath Japan. The subducting Pacific and PHS slabs were imaged as dipping high-velocity (high-V) zones, whereas low-velocity (low-V) anomalies are revealed in the surrounding mantle, in particular, in the mantle wedge above the slabs.

A simultaneous inversion of different sets of teleseismic arrival-time data recorded by separate arrays deployed in different areas (and perhaps in different periods) may result in a distorted tomography, because teleseismic tomography uses relative travel-time residuals of teleseismic events which mainly reflect the relative velocity anomalies beneath an array which recorded the teleseismic events (Zhao et al., 1994, 2012). Hence, it would be much better to use only the data from those teleseismic events which were recorded by a complete seismic network (such as the Hi-net) which covers the entire study region densely and uniformly.

Another problem of the previous studies (Zhao et al., 1994, 2012; Abdelwahed and Zhao, 2007; Asamori and Zhao, 2015) is that the teleseismic data used were much fewer than the local-earthquake data used in the tomographic inversion. Thus, the crust and upper mantle down to ~200 km depth were densely sampled by both the local and teleseismic rays, whereas the deeper areas were much less sampled by the teleseismic rays alone. This problem would have also affected the quality of the previous tomographic models beneath Japan, in particular, for the areas deeper than ~200 km.

In the present study, we have made great efforts to measure hundreds of thousands of high-quality P- and S-wave arrival-time data from many teleseismic events recorded by the Hi-net during the past 10 years. The number of the newly collected teleseismic data is even greater than that of the local-earthquake data used in this study. A joint inversion of both the local and teleseismic data results in robust Vp and Vs tomography of the crust and mantle down to 700 km depth of the entire Japan subduction zone. In addition, we also study the 3-D Vs structure beneath Japan by a joint inversion of the local and teleseismic S-wave arrival times and Rayleigh-wave phase-velocity data at periods of 20–150 s obtained by this study. Because we have collected and used much more body-wave and surface-wave data than all the previous tomographic studies in this region, we have obtained much more robust results, such as a clearly imaged Pacific slab with a thickness of ~100 km from a 1-D starting velocity model. The present results shed important new light on the deep structure and dynamics of the Japan subduction zone.

2. Data

In this study we used 1852 seismic stations installed on the Japan Islands (Fig. 2a), which include 796 Hi-net stations (Fig. 2b), 74 F-net broadband stations (Fig. 2c), and 982 JMA (Japan Meteorological Agency) and Japanese national university stations (J-Array). We used three sets of data to conduct tomographic inversions. The first data set contains P- and S-wave arrival times of 2528 local earthquakes which occurred in and around the Japan Islands (Fig. 2d). The second data set contains P-wave relative travel-time residuals of 747 teleseismic events and S-wave residuals of 643 teleseismic events (Fig. 2e). The third data set consists of fundamental mode Rayleigh-wave amplitude and phase data in a period range of 20–150 s from 1030 teleseismic events (Fig. 2f).

Among the great number of local earthquakes recorded by the dense seismic network (Fig. 2a), we selected a best set of events for our tomographic study. The study area is divided into many cubic blocks with a size of $50 \times 50 \times 10$ km^3. The local events are selected by a specific scheme of selection according to the maximum number of recording stations and the minimum formal uncertainty of the hypocenter locations. The shallow offshore events were removed from the data set because of their poor hypocentral locations. As a result, 2528 local events are selected (Fig. 2d), which generated 501,571 P-wave and 220,340 S-wave arrival times. The picking accuracy is estimated to be 0.05–0.10 s for P-wave data and 0.05–0.15 s for S-wave data. This data set contains more P- and S-wave arrivals than those released by the JMA Unified Earthquake Catalog, thanks to the great efforts made by the staff members of Tohoku University who picked up all the clear P and S arrivals from the original three-component seismograms. The uncertainty of hypocenter locations is <5 km for all the events and <3 km for the events beneath the seismic network.

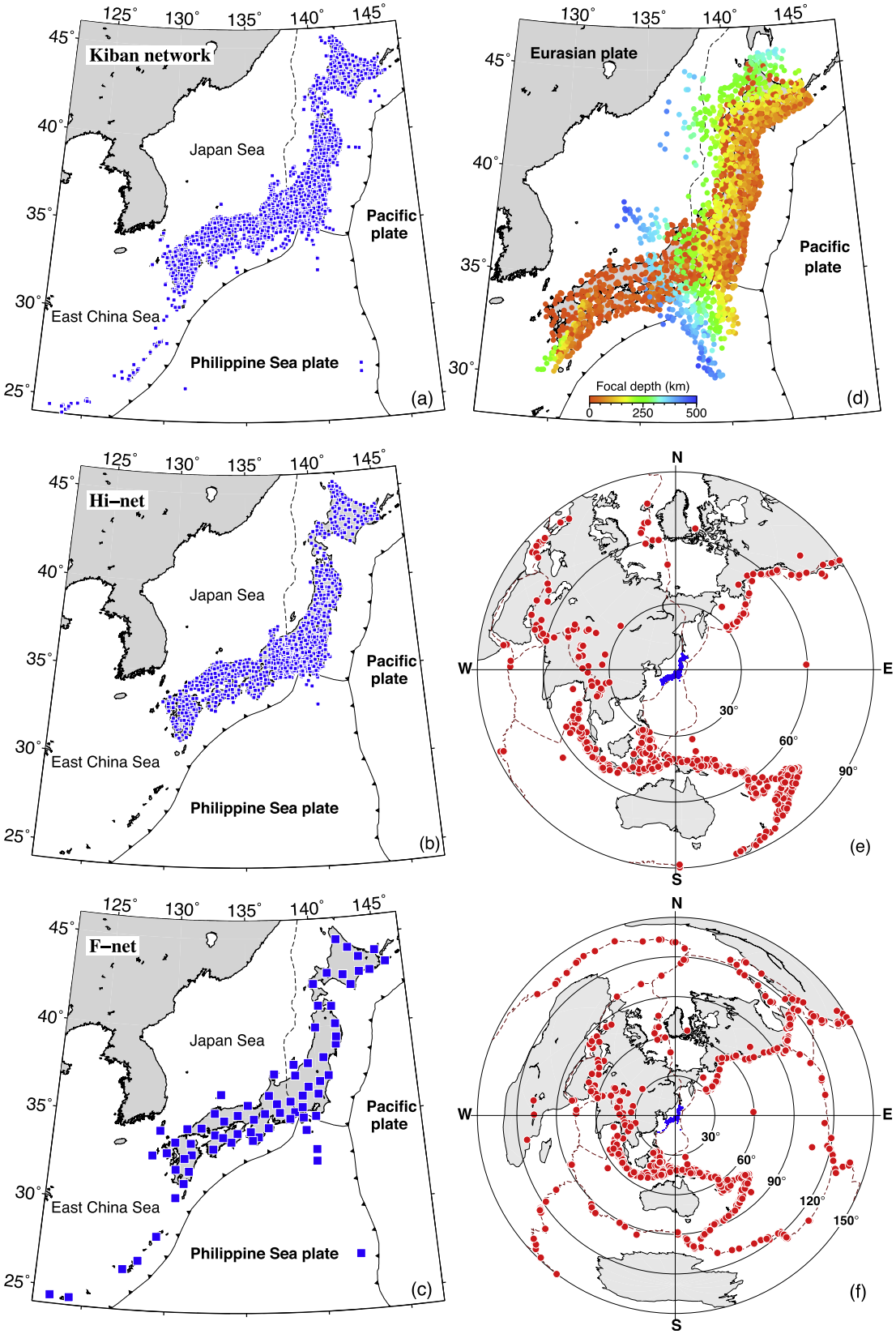

Fig. 2. Distribution of seismic stations of (a) the Kiban seismic network, (b) the High-sensitivity seismic network (Hi-net), and (c) the F-net. Epicentral distribution of (d) the local earthquakes and (e) the teleseismic events used for body-wave tomography, and (f) the teleseismic events used for Rayleigh-wave phase velocity tomography. The colors in (d) denote the focal depth whose scale is shown on the map. (For interpretation of the references to colour in this figure legend, the reader is referred to the web version of this article.)

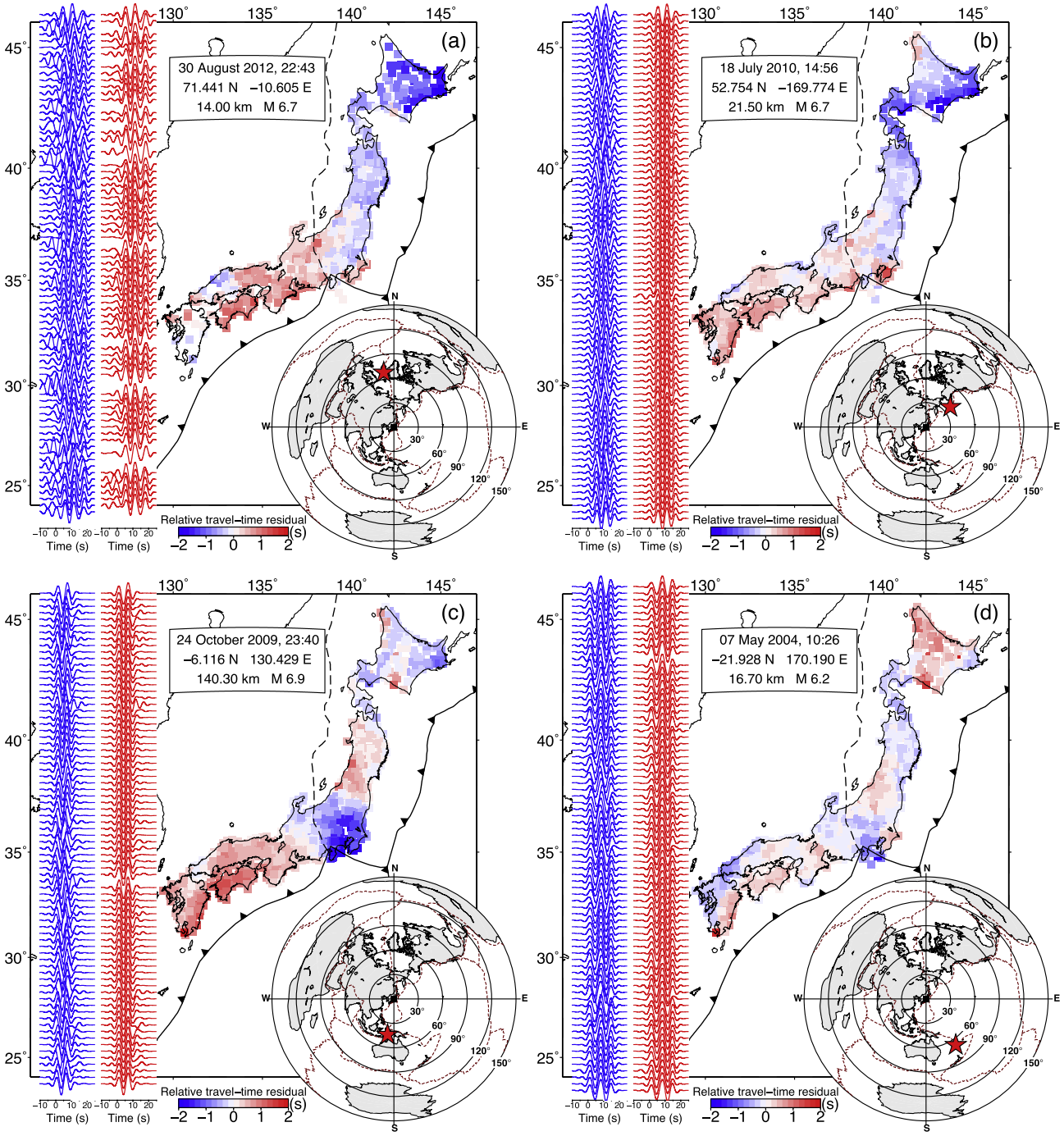

Fig. 3. Distributions of P-wave relative travel-time residuals of four teleseismic events (red stars) used in this study. The color squares show the seismic stations used. The red and blue colors denote delayed and early arrivals, respectively. The scale for the relative residuals is shown below each panel. The blue and red waveforms beside each map show seismograms before and after the alignment, respectively (see text for details). Hypocenter parameters of each teleseismic event are shown above each map. (For interpretation of the references to color in this figure legend, the reader is referred to the web version of this article.)

We newly measured 505,452 P-wave and 251,958 S-wave relative travel-time residuals from 747 and 643 teleseismic events, respectively (Fig. 2e) using the multi-channel cross-correlation technique (VanDecar and Crosson, 1990). These data are collected precisely from the high-quality three-component seismograms recorded by the Hi-net seismic stations (Fig. 2b) during April 2004 to December 2014. The P-wave relative travel-time residuals are measured from the vertical-component seismograms filtered in a frequency band of 0.1–0.2 Hz (Fig. 3), whereas the S-wave relative residuals are collected from the horizontal-component seismograms filtered in a frequency band of 0.01–0.1 Hz (Fig. 4). The teleseismic events used in this study are $\geqslant M$ 6.0, and their epicentral distances are in a range of ~30–90°. Hypocentral parameters of the teleseismic events are obtained from the Bulletins of the International Seismological Center (ISC). The azimuthal coverage of these events is very good in all directions except for the Pacific Ocean, and most of the events occurred in subduction zones (Fig. 2e).

We also newly measured the amplitudes and phases of fundamental mode Rayleigh waves in a period range of 20–150 s from

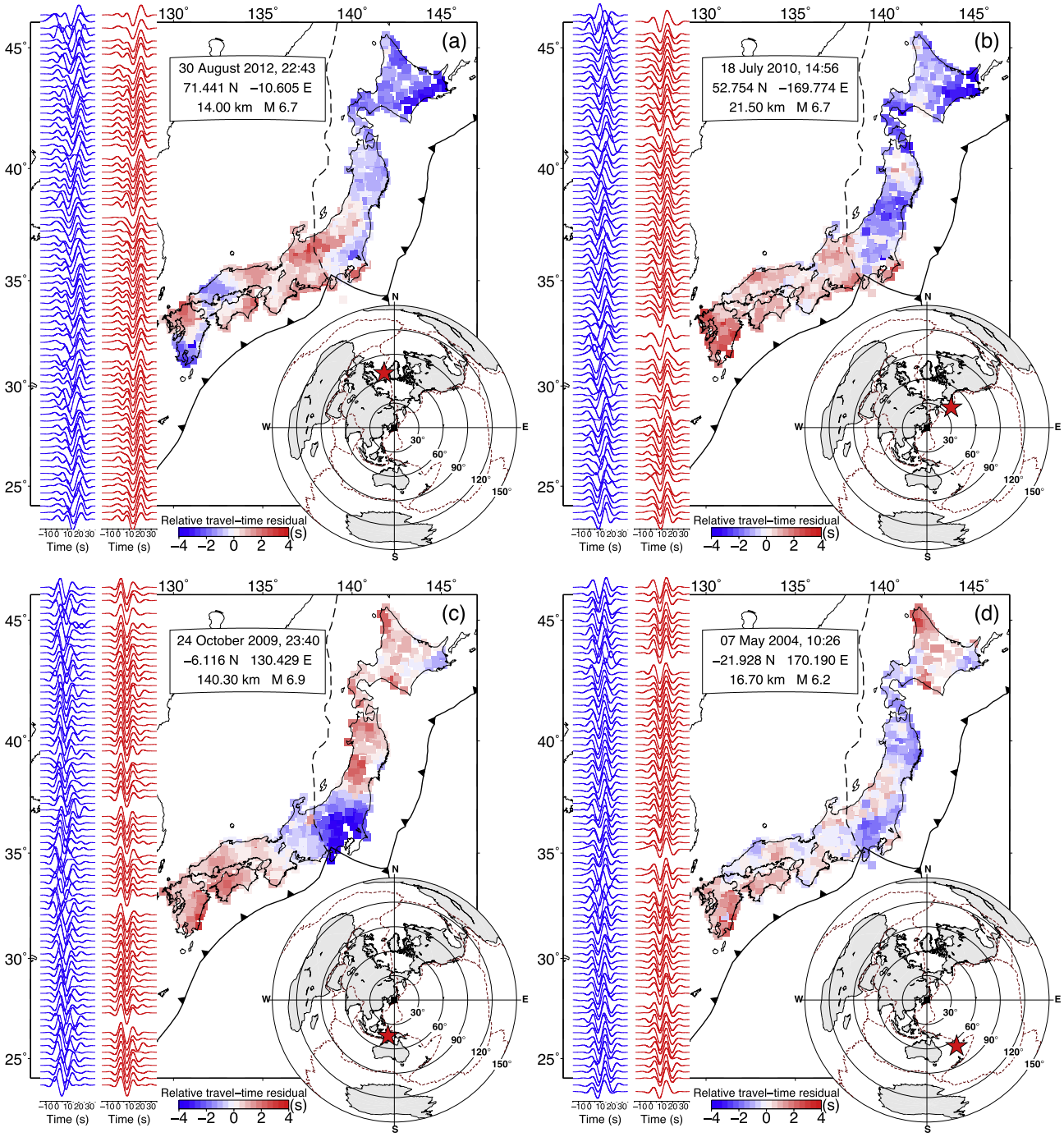

Fig. 4. The same as Fig. 3 but for S waveforms and S-wave relative travel-time residuals of four teleseismic events (red stars) used in this study. (For interpretation of the references to color in this figure legend, the reader is referred to the web version of this article.)

vertical-component seismograms of 1030 well-selected teleseismic events (focal depths <100 km; $M \geqslant 6.0$) with epicentral distances of ~30–150° (Fig. 2f), which were recorded by 74 permanent F-net broadband stations (Fig. 2c) during April 2004 to December 2014. Hypocentral parameters of the 1030 teleseismic events are also obtained from the ISC bulletins. At first, the Rayleigh waves are isolated by applying adaptive time windows to broadband vertical-component seismograms after correcting for the instrument response (Fig. 5a). The time windows are selected in a group velocity range of 2.6–5.2 km/s. The red trace in Fig. 5a shows a windowed broadband Rayleigh wave of a teleseismic event (M 6.1, 37.9 km depth) on 29 December 2014 beneath the Philippine Islands (the red star in Fig. 5c) recorded at F-net station FUJ (the blue square in Fig. 5c). The windowed broadband seismogram (the red trace in Fig. 5a) is then filtered into 28 different period bands from 15 to 150 s with a period-dependent Gaussian band-pass filter. The blue traces in Fig. 5a show the obtained Gaussian-filtered Rayleigh waves at 23 periods. Then envelops of the Gaussian-filtered Rayleigh waves are calculated, and the normalized amplitudes of the obtained envelops are shown in Fig. 5b. Based on the theoretical group velocity (the green line in Fig. 5b) calculated for the PREM model (Dziewonski and Anderson, 1981), we selected the optimal group velocity at each period with a clear and large enough normalized amplitude peak

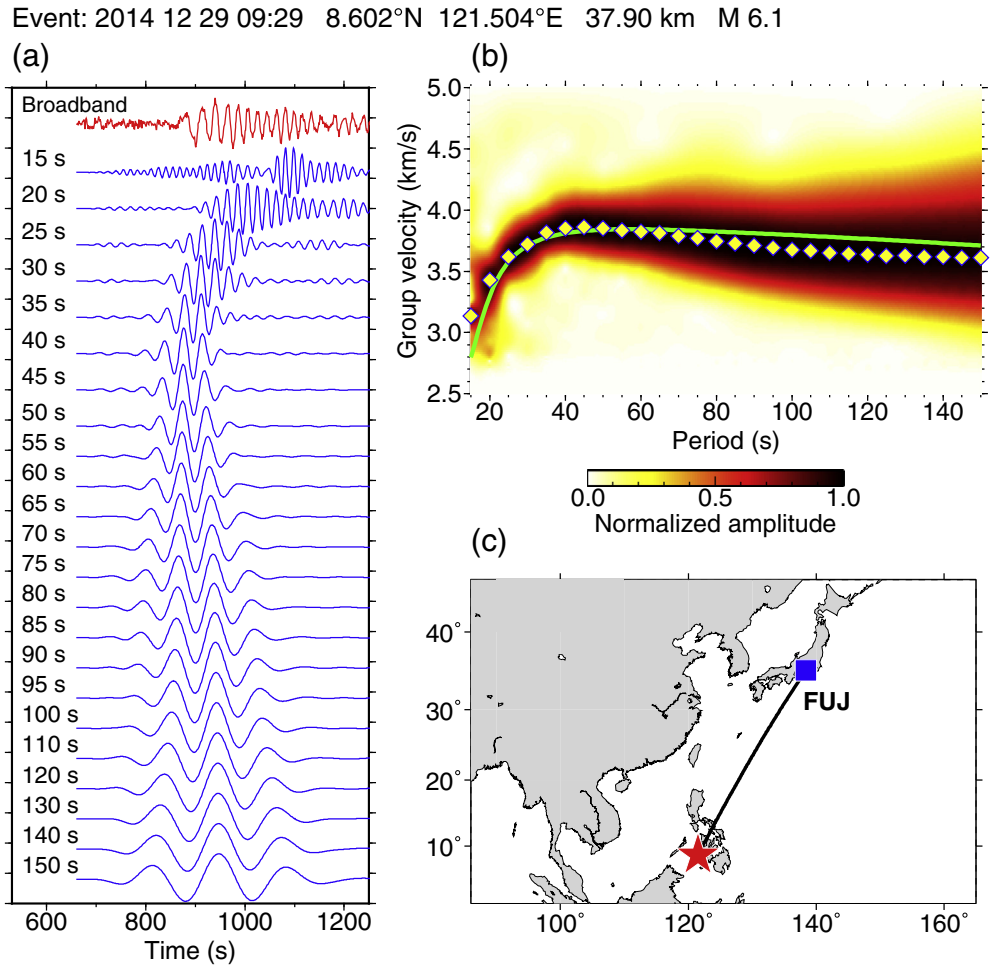

Fig. 5. An example of measuring the Rayleigh-wave group velocity. The amplitudes and phases of the Gaussian-filtered Rayleigh waves are then determined at group arrival times by Fourier analysis. For details, see the data processing section.

(>0.7) (the yellow diamond symbols in Fig. 5b). Then, following the approach of Forsyth and Li (2005), we determined the amplitudes and phases of the Gaussian-filtered Rayleigh waves at group arrival times by Fourier analysis. The obtained amplitudes for each event are normalized by the root-mean-square (RMS) amplitude of each event. The phase data are corrected by a reference station phase for each event to reduce the effect of hypocentral mislocations of the teleseismic events. To obtain a robust result, we adopted only those events which were recorded by more than 20 seismic stations at each period. As a result, the number of amplitude and phase data pair measured at each period ranges from 46,926 to 55,579.

3. Method

3.1. Body-wave tomography

We used the tomographic method of Zhao et al. (1994, 2012) to invert the local-earthquake arrival times and the teleseismic relative travel-time residuals simultaneously for 3-D Vp and Vs models beneath the study region. This method includes a forward scheme that can deal with a general velocity model in which complex velocity discontinuities exist and seismic velocity changes in three dimensions (Zhao et al., 1994, 2012). To express the 3-D velocity structure, a 3-D grid is set up in the modeling space, and velocity perturbations from a starting 1-D velocity model at every grid nodes are taken as unknown parameters. Grid meshes are arranged at 10, 25, 40 to 700 km depths with a vertical grid interval of 25 km from 40 to 665 km depths (Fig. S1). The grid interval is 0.33° in the horizontal direction. The starting 1-D velocity model (Fig. S2) is derived from the CRUST1.0 model (Laske et al., 2013) and the IASP91 Earth model (Kennett and Engdahl, 1991). The velocity perturbation at any point in the model is computed by linearly interpolating the velocity perturbations at the eight grid nodes surrounding that point. An efficient 3-D ray tracing technique (Zhao et al., 1992) is used to compute theoretical travel times and ray paths.

For a teleseismic event, the ray from the hypocenter to a receiver is firstly traced for the IASP91 Earth model, and the intersection between the ray and the bottom plane of the modeling space is found (Zhao et al., 1994). Then the ray path between the intersection and the receiver is determined using the 3-D ray tracing technique (Zhao et al., 1992). The relative travel-time residual of a teleseismic event is related to velocity anomalies along the ray path between the intersection and the receiver (Zhao et al., 1994).

The depths of crustal layers in the CRUST1.0 model (Laske et al., 2013) and station elevations are taken into account in the 3-D ray tracing. The LSQR algorithm (Paige and Saunders, 1982) is adopted to solve the observation equations relating the observed local-earthquake arrival times and the teleseismic relative travel-time residuals to the unknown velocity parameters. Smoothing and damping regularizations are adopted to suppress the dramatic short-scale variations of velocity anomalies in the study region (Zhao et al., 2012). The final tomographic results are obtained after

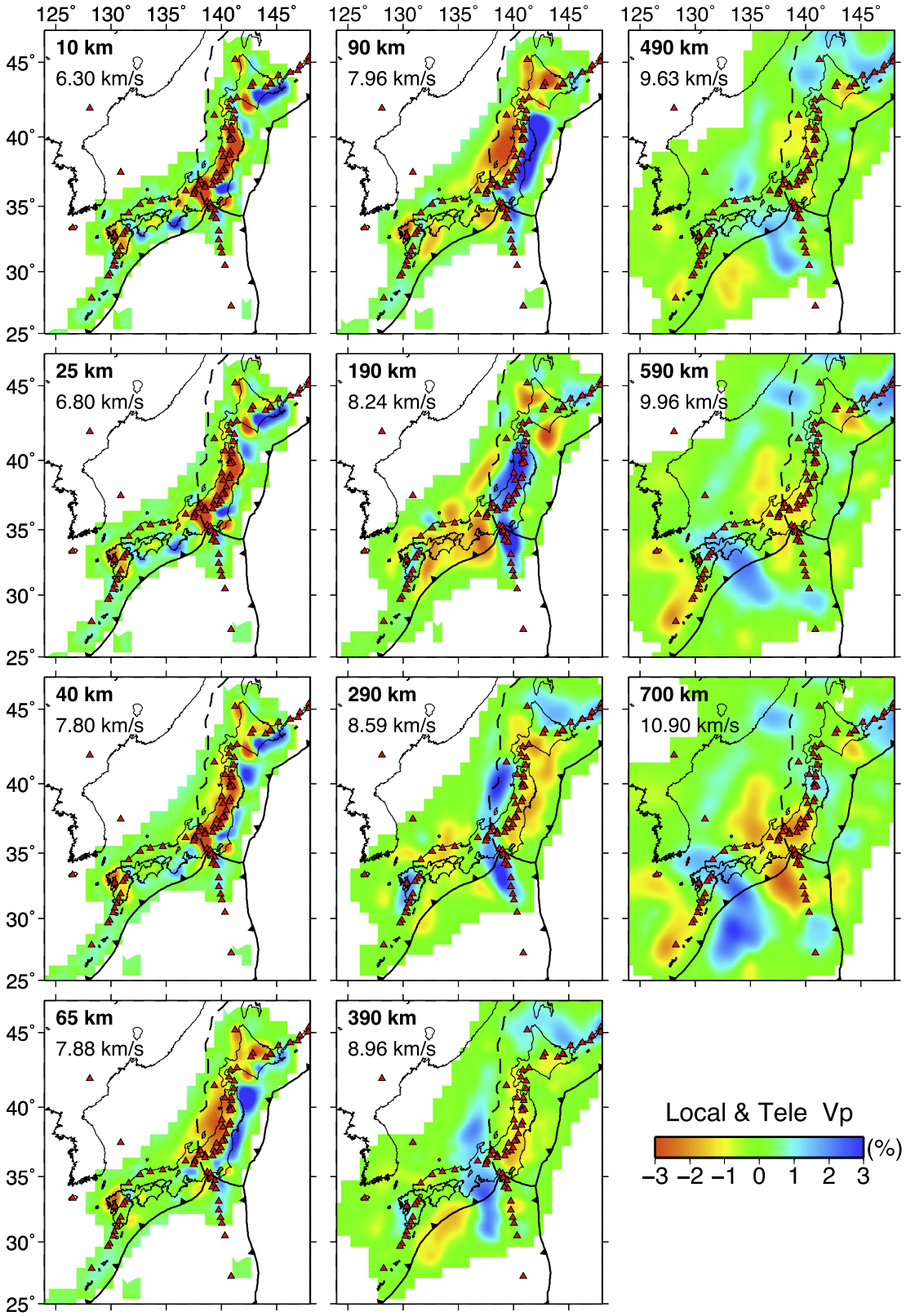

Fig. 6. Map views of Vp tomography obtained by inverting the P-wave travel-time data of both local earthquakes and teleseismic events. The layer depth and the average velocity at that depth are shown in each map. The red and blue colors denote low and high velocities, respectively. The velocity perturbation (in %) scale is shown at the bottom. The other labeling is the same as that in Fig. 1. (For interpretation of the references to color in this figure legend, the reader is referred to the web version of this article.)

ten iterations (Table S1). Hypocentral parameters of local earthquakes and relative travel-time residuals of teleseismic events are re-determined for the obtained 3-D velocity model after each iteration. To minimize the effect of uncertainties of the initial velocity model, the final velocity perturbation at each grid node is calculated from the average of the obtained velocity perturbations

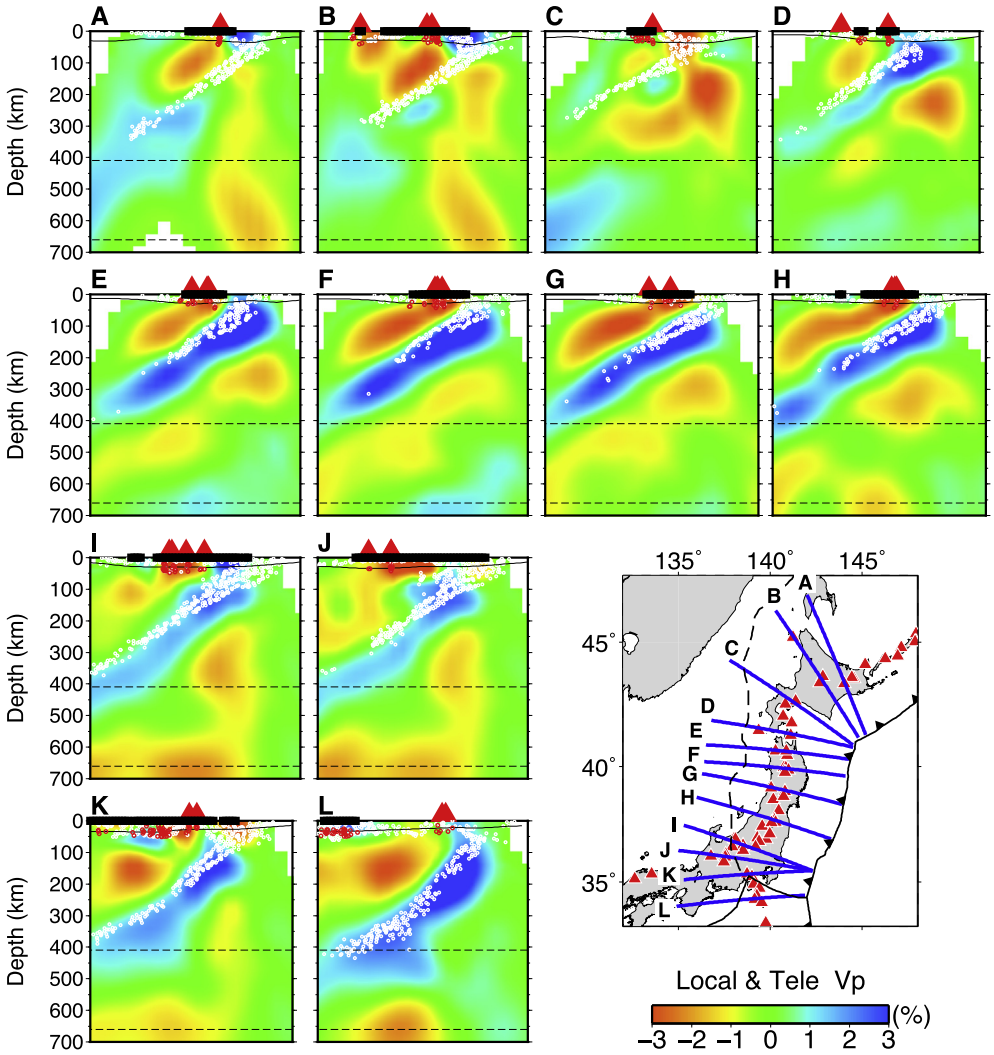

Fig. 7. Vertical cross-sections of Vp tomography along the profiles (blue lines) shown on the inset map. This 3-D Vp model is obtained by inverting the P-wave travel-time data of both local earthquakes and teleseismic events. The red and blue colors denote low and high velocities, respectively. The velocity perturbation (in %) scale is shown below the map. The red triangles denote the active and Quaternary volcanoes. The black bar atop each cross-section denotes the land area. The background seismicity and low-frequency micro-earthquakes which occurred within a 20-km width of each profile are shown in white and red circles, respectively. In each panel, the curved black line shows the Moho discontinuity, and the two dashed lines denote the 410 and 660 km discontinuities. (For interpretation of the references to color in this figure legend, the reader is referred to the web version of this article.)

at each depth. In this study, the finite-frequency effect is not taken into account for the body-wave tomographic inversion. The finite-frequency effect may influence the tomographic inversion of long-period body-wave and surface-wave data (e.g. Dahlen et al. (2000), Hung et al. (2000)), but the effect is very small for the inversion of short-period body-wave travel-time data as used in this study, and the ray and finite-frequency approaches result in essentially the same tomographic images, as shown clearly by Tong et al. (2011, 2012).

3.2. Surface-wave tomography

The teleseismic Rayleigh-wave amplitude and phase data we measured are used to determine fundamental mode Rayleigh-wave phase-velocity models in a period range of 20–150 s for the Japan subduction zone. To account for multipath interference effects caused by heterogeneities outside the modeling space, we adopted the two-plane-wave (TPW) interference technique developed by Forsyth and Li (2005) who showed that the incoming Rayleigh wave at each period from a teleseismic event can be regarded as the sum of two horizontally-propagating plane waves. Thus the incoming wavefield at each period is described by six parameters: the amplitude, reference phase and direction of each of two plane waves. Following the TPW method, we minimize residuals of the real and imaginary components rather than match the observed amplitude and phase data during the inversion. We first determined six best fitting wave parameters for each event in a least-squares sense using a downhill simplex method of simulated annealing (Press et al., 1992), with the finite-frequency effects taken into account (Yang and Forsyth, 2006). Then we conducted a tomographic inversion for 2-D Rayleigh-wave phase velocities in the study region by fixing the obtained best-fitting wave parameters. For each period, we set up a 2-D grid in the study region following the approach of Zhao et al. (1992, 2012). Rayleigh-wave phase-velocity perturbations at every grid nodes from a 1-D phase-velocity model derived from PREM (Dziewonski and Anderson, 1981) are taken as unknown parameters. The phase-velocity perturbation at any point in the model is computed by linearly interpolating the phase-velocity perturbations at the four grid nodes surrounding that point. The LSQR algorithm (Paige and Saunders, 1982) is adopted to solve the observation equations relating the observed real and imaginary components residuals to

the unknown phase-velocity parameters. Smoothing and damping regularizations (Zhao et al., 2012) are adopted to suppress the dramatic short-scale phase-velocity variations. The final tomographic results for each period are obtained after twenty iterations. The best-fitting wave parameters of each teleseismic event are re-determined for the obtained 2-D phase-velocity model after each iteration. To minimize the effect of uncertainties of the initial phase-velocity model, the final phase-velocity perturbation at each grid node is calculated from the average phase-velocity obtained for each period.

3.3. Joint inversion of body-wave and surface-wave data

To constrain better the 3-D Vs structure of the Japan subduction zone, we modified the tomographic method of Zhao et al. (1994, 2012) to conduct joint inversions of our S-wave travel-time data of local earthquakes and teleseismic events and the Rayleigh-wave phase-velocity data at periods of 20–150 s.

The Rayleigh-wave phase-velocity perturbation $\frac{\delta c(k)}{c}$ at position x and period k is related to the 1-D velocity and density structure beneath position x as

$$\frac{\delta c(k)}{c} = \int_0^R \left[K_\rho(k,r)\frac{\delta\rho(r)}{\rho} + K_\alpha(k,r)\frac{\delta\alpha(r)}{\alpha} + K_\beta(k,r)\frac{\delta\beta(r)}{\beta} \right] dr, \quad (1)$$

where R is the radius of the Earth, $\frac{\delta\rho(r)}{\rho}$, $\frac{\delta\alpha(r)}{\alpha}$ and $\frac{\delta\beta(r)}{\beta}$ are perturbations of density, Vp and Vs at radius r, respectively, whereas $K_\rho(k,r)$, $K_\alpha(k,r)$ and $K_\beta(k,r)$ are the corresponding sensitivity kernels at radius r and period k (e.g. Zhang and Tanimoto (1993), Yoshizawa et al. (2010)). The Rayleigh-wave phase velocity is much more sensitive to Vs than to Vp and density (e.g. Saito (1988)), and so we only performed inversions for 3-D Vs perturbations and fixed the density and Vp to those of the initial model. Thus, Eq. (1) is simplified as:

$$\frac{\delta c(k)}{c} = \int_0^R K_\beta(k,r)\frac{\delta\beta(r)}{\beta} dr, \quad (2)$$

where the sensitivity kernel $K_\beta(k,r)$ and the predicted phase velocity are calculated using the code DISPER80 (Saito, 1988).

Following Eq. (2), in the joint tomographic inversion, we assume that the Rayleigh-wave phase-velocity residual at each period and position x mainly reflects the 1-D Vs structure beneath position x down to 600 km depth. This scheme is similar to that dealing with the relative travel-time residuals of a teleseismic event as mentioned above (Zhao et al., 1994, 2012). A 3-D grid is set up in the modeling space (Fig. S1), and Vs perturbations at every grid nodes from a starting 1-D Vs model are taken to be unknown parameters following the method of Zhao et al. (1994, 2012). The Vs perturbation at any point in the modeling space is computed by linearly interpolating the Vs perturbations at the eight grid nodes surrounding that point. The starting 1-D Vs model is derived from the CRUST1.0 and the IASP91 models (Fig. S2). The initial Vp model is derived from the optimal 3-D Vp model obtained by inverting the P-wave travel-time data of both local earthquakes and teleseismic events in this study. The initial density model is derived from the PREM model. The

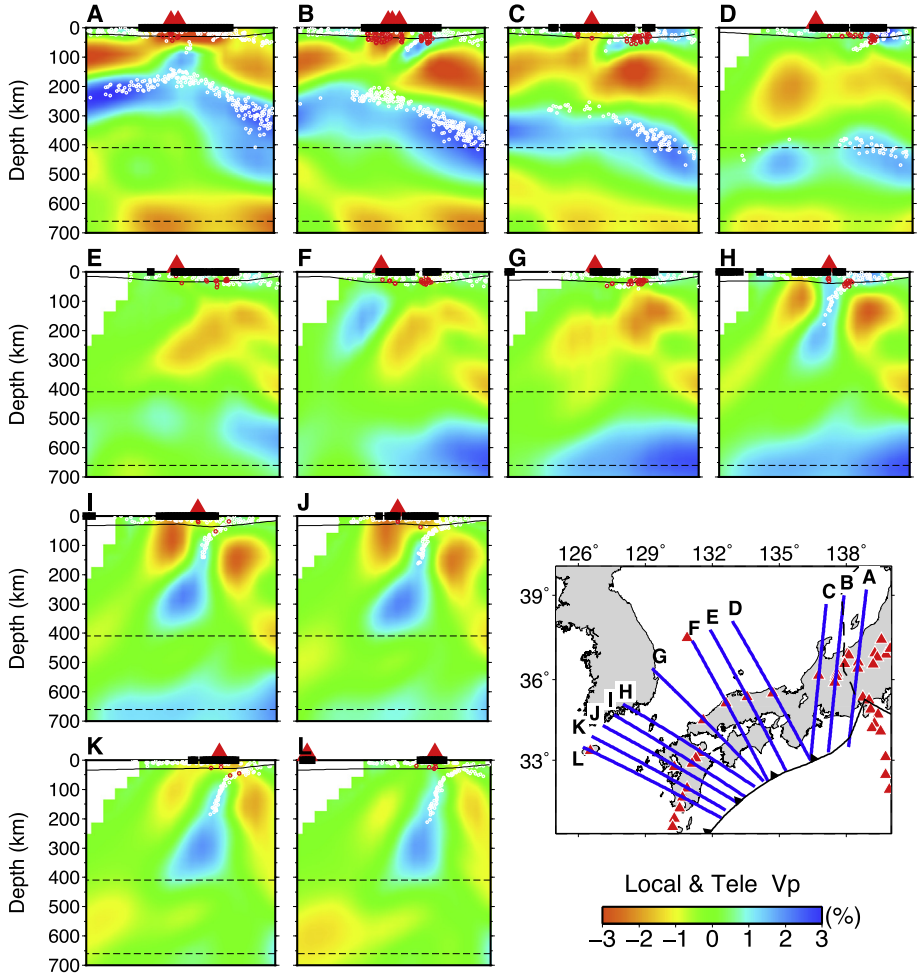

Fig. 8. The same as Fig. 7 but for vertical cross-sections beneath SW Japan.

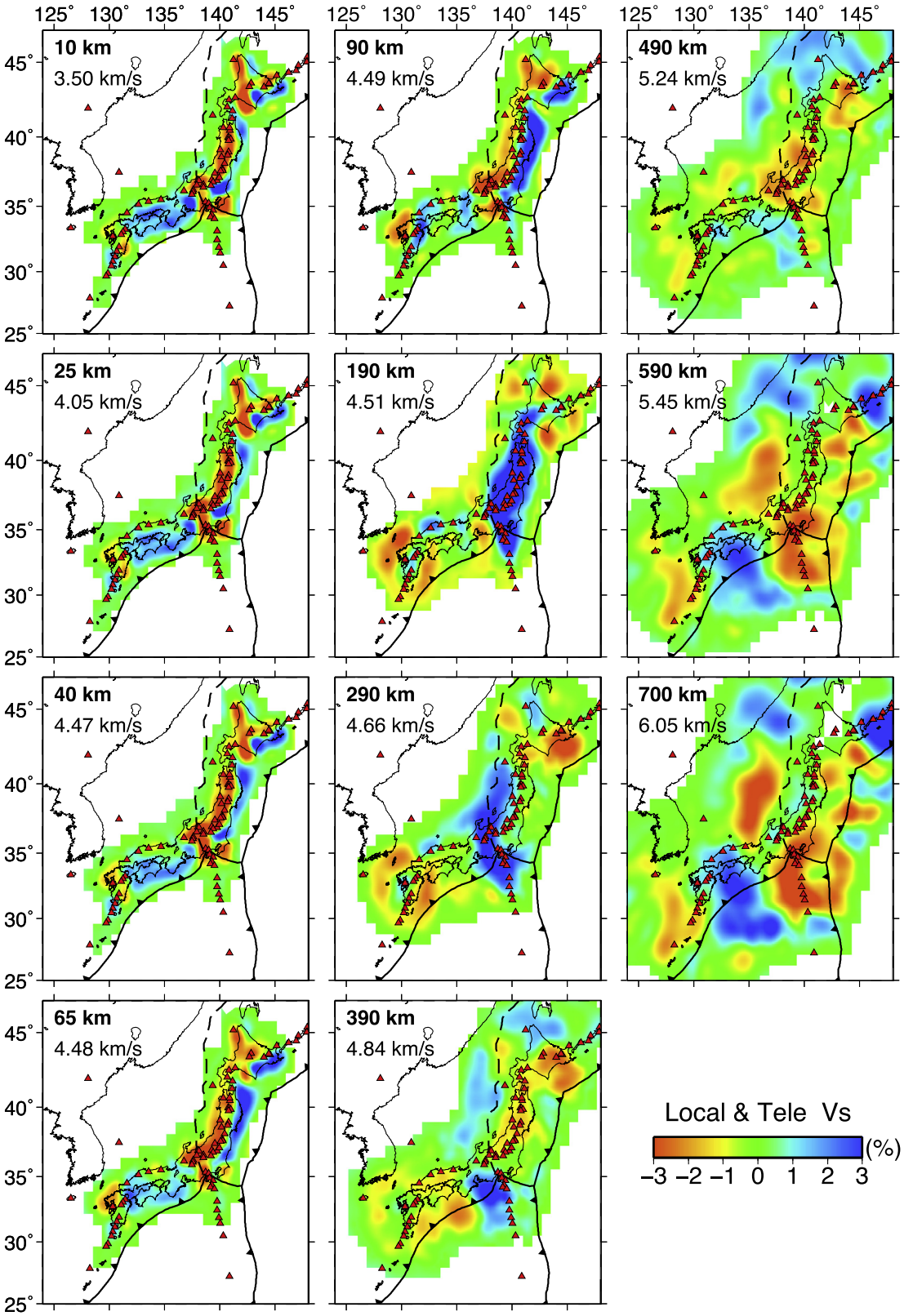

Fig. 9. The same as Fig. 6 but for Vs tomography obtained by inverting the S-wave travel-time data of both local earthquakes and teleseismic events.

local-earthquake S-wave travel-time residuals, teleseismic S-wave relative travel-time residuals, and the Rayleigh-wave phase-velocity residuals at periods of 20–150 s form a whole set of observed data. The LSQR algorithm is adopted to solve the observation equations relating the observed data to the unknown Vs parameters. Smoothing and damping regularizations (Zhao et al., 2012) are adopted to suppress the dramatic short-scale Vs variations. The final tomographic results are obtained after ten iterations

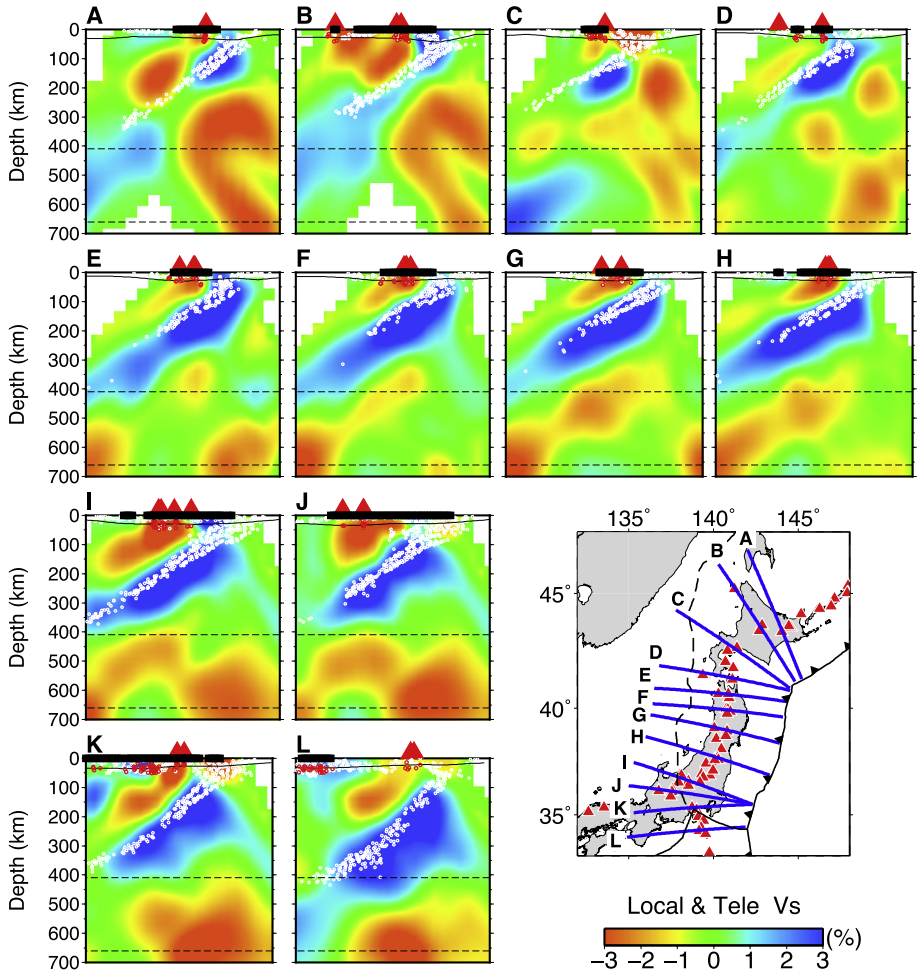

Fig. 10. The same as Fig. 7 but for Vs tomography obtained by inverting the S-wave travel-time data of both local earthquakes and teleseismic events.

(Table S1). To minimize the effect of uncertainties of the initial Vs model, the final Vs perturbation at each grid node is calculated from the average of the obtained Vs perturbations at each depth.

A critical issue of the joint inversion of body-wave and surface-wave data is to find the optimal relative weights for the body-wave and surface-wave data in the inversion. This issue exists in all studies dealing with a joint inversion of different kinds of geophysical data (e.g. Lees and VanDecar (1991), Villagómez et al. (2014), Zhang et al. (2014), Syracuse et al. (2015)). In this study, we conducted many tomographic inversions with different relative weights to find the optimal one. We finally adopted an optimal relative weight of 20.0 for the surface-wave data by considering the balance of the body-wave and surface-wave data (Table S1), because our data set contains much more body-wave data than the surface-wave data.

4. Analysis and results

4.1. Body-wave tomography

Figs. S3 and S4 show the distributions of P- and S-wave ray paths in different depth ranges from all the local and teleseismic events used in this study, indicating that both P- and S-rays criss-cross very well under the study region down to ~700 km depth.

To assess the adequacy of ray coverage and to evaluate the resolution of the tomographic images, we conducted many checkerboard resolution tests (CRTs) following the approach of Zhao et al. (1994, 2012). To perform a CRT, we first assigned positive and negative velocity perturbations of 3% to all the 3-D grid nodes, then calculated synthetic residuals for the checkerboard model with the same numbers of seismic stations, events and ray paths as those in the real data set, and then inverted the synthetic data to see whether the input checkerboard model could be recovered or not. To simulate the picking errors contained in the observed data, random noise with a normal distribution having a standard deviation of 0.1 s was added to the synthetic travel-time data before the tomographic inversion. Figs. S5 and S6 show the test results for the Vp and Vs tomography, respectively, with a lateral grid interval of 0.33°, which are obtained by inverting the travel-time data of local and teleseismic events simultaneously. These test results indicate that our Vp and Vs models have a resolution of ~30 km in the horizontal direction and 15–25 km in depth.

We conducted many tomographic inversions to find the optimal values of the damping, smoothing and iteration parameters. The optimal values of these parameters are shown in Table S1. The RMS travel-time residuals for the P- and S-wave data of local and teleseismic events are reduced significantly after the joint inversions (Fig. S7a–d). In the optimal tomographic model, the lateral grid interval is 0.33°. Figs. 6–12 show the optimal tomographic results which are obtained by inverting the travel-time data of local earthquakes and teleseismic events simultaneously. These results show that the obtained Vp and Vs images are generally similar to each other. The subducting Pacific and PHS slabs are imaged clearly as dipping high-V zones, whereas obvious low-V anomalies are revealed in the surrounding mantle, in particular, in the mantle wedge above the slabs.

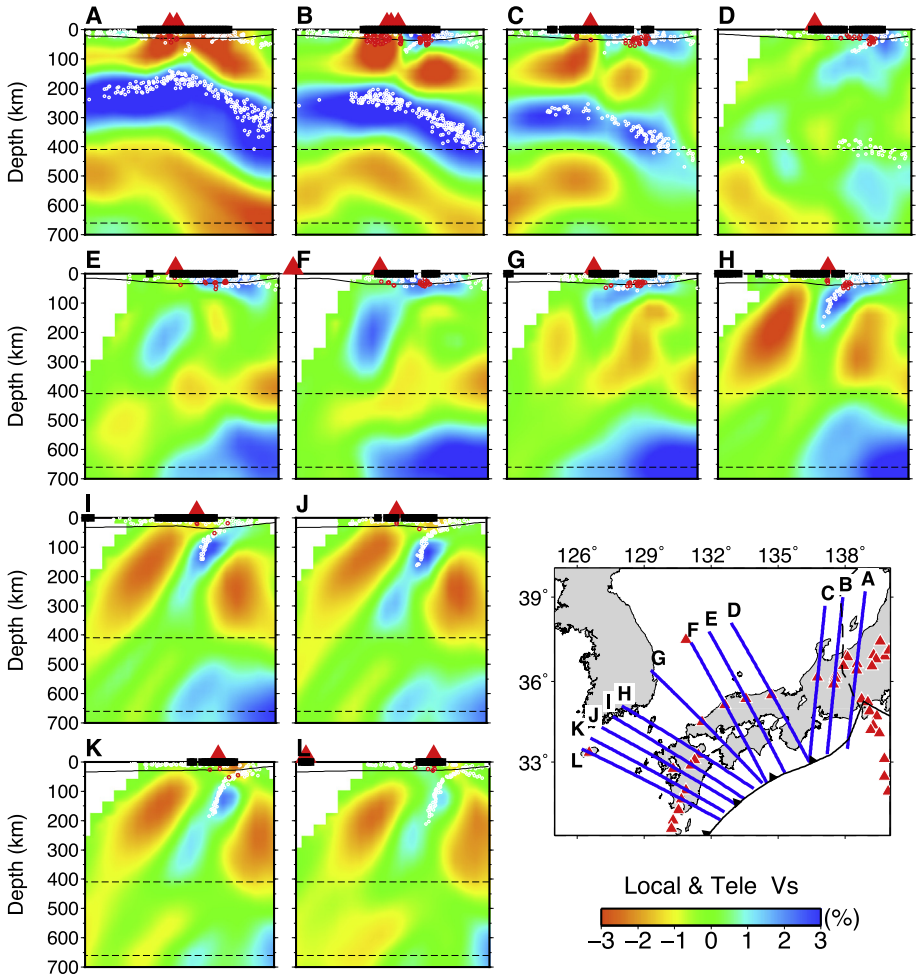

Fig. 11. The same as Fig. 10 but for vertical cross-sections beneath SW Japan.

We also conducted restoring resolution tests (RRTs) (Zhao et al., 1994, 2012) to confirm the obtained 3-D Vp and Vs images. The procedure of the RRT is the same as that of the CRT, except for the input model. The obtained tomographic results (Figs. 7, 8, 10 and 11) are adopted as the input model. Random errors with a normal distribution having a standard deviation of 0.1 s were added to the synthetic data before the tomographic inversion. The RRT results (Figs. S8–S11) show that the main features of the tomographic images are well recovered, suggesting that the velocity anomalies revealed are reliable features.

With the obtained 3-D Vp and Vs models, we determined Poisson's ratio (σ) images beneath the study region using the relation $(Vp/Vs)^2 = 2(1-\sigma)/(1-2\sigma)$ (Zhao et al., 1996) (Figs. 12, S12–14). The subducting Pacific and PHS slabs generally exhibit low Poisson's ratio (low-σ), whereas high Poisson's ratio (high-σ) anomalies are generally visible in the surrounding mantle.

To further ensure the robustness of our tomographic results, we used only the local-earthquake arrival-time data to conduct Vp and Vs tomography. The RMS travel-time residuals of both the P- and S-wave data are reduced significantly after the tomographic inversions (Fig. S15a,c). The CRT results (Figs. S16 and S17) show that inverting the local-earthquake arrival-time data can only recover the velocity anomalies down to ~400 km depth. Figs. 12a, b and S18–S23 show the corresponding Vp and Vs images obtained. The pattern of the images obtained from the local-event data alone is similar to that of the shallow part of the tomography obtained by the local and teleseismic joint inversions (Figs. 6–12).

In addition, we also inverted only the teleseismic data for the 3-D Vp and Vs structure. The RMS residuals of both P- and S-wave teleseismic data are reduced significantly after the inversions (Fig. S15b,d). As compared with the local event data, the teleseismic data can constrain the deeper structure of the study region. However, the teleseismic data cannot well constrain the shallow structure (<100 km depth), because the teleseismic rays are close to vertical in the shallow part where the rays do not crisscross very well (Figs. S24 and S25). Figs. 12c,d and S26–S31 show the Vp and Vs images thus obtained. The main pattern of the teleseismic tomography at depths >100 km is similar to that of the images obtained by the local and teleseismic joint inversion (Figs. 6–12).

4.2. Surface-wave tomography

Fig. S32 shows ray density distributions of the fundamental mode Rayleigh-wave data measured from the 1030 teleseismic events (Fig. 2f) used in this study. The rays at periods of 20–150 s crisscross very well in and around the Japan Islands.

We conducted many CRTs to assess the adequacy of the ray coverage and to evaluate the spatial resolution of the phase-velocity tomographic images. To perform a CRT, we first assigned positive and negative phase-velocity perturbations of 3% to all the 2-D grid nodes, then calculated synthetic real and imaginary components residuals for the 2-D checkerboard model with the same numbers of seismic stations, teleseismic events and ray paths as those in the real data set. The synthetic data are then inverted to investigate

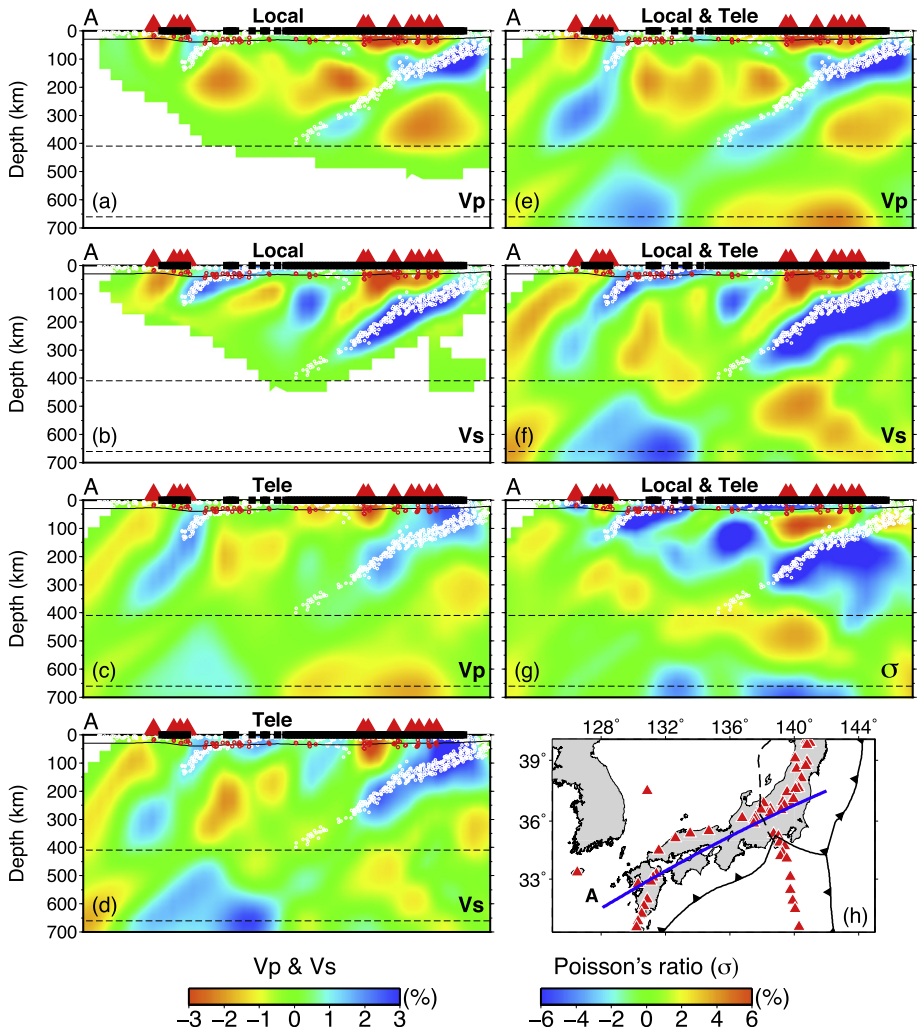

Fig. 12. Vertical cross-sections of (a, c, e) Vp, (b, d, f) Vs and (g) Poisson's ratio images along the profile (blue line) shown on the inset map (h), which are determined by inverting the local earthquake data (a, b), teleseismic data (c, d), and a joint inversion of the local and teleseismic data (e, f, g). The other labeling is the same as that in Fig. 7. (For interpretation of the references to color in this figure legend, the reader is referred to the web version of this article.)

whether the assigned phase-velocity anomalies could be recovered or not. Fig. S33 shows the test results for the phase-velocity tomography at 11 different periods. These test results indicate that our phase-velocity tomographic models have a resolution of ~30 km in and around the Japan Islands.

Fig. 13 shows the final results of the Rayleigh-wave phase-velocity tomography. The RMS residuals of the real and imaginary components data at periods of 20–150 s are reduced significantly after the tomographic inversions (Fig. S34). In the optimal tomographic models, the grid interval is 0.33° in the E–W and N–S directions for all the period bands. Strong lateral phase-velocity variations are revealed in the study region. The phase-velocity images at the short periods reflect well the crustal structure (e.g. Zhao et al. (2012), Liu et al. (2013a,b)) and the surface geological features, such as the distribution of active volcanoes, islands and oceanic regions, etc. At the long periods, the tomographic images reflect the deeper structure in the upper mantle, such as the cold subducting slabs and the hot mantle wedge (Fig. 13).

The obtained Rayleigh-wave phase-velocity data (Fig. 13) are inverted for the 3-D Vs structure of the study region (Figs. S35–S37). The RMS residual of the Rayleigh-wave phase-velocity data is reduced significantly after the inversions (Fig. S7e). We conducted extensive synthetic tests to know the vertical resolution of the obtained 3-D Vs tomography. The synthetic test results (e.g., Fig. S38) show that the 3-D Vs model has a vertical resolution of ~50 km at depths of 0–150 km and ~100 km at depths of ~150–350 km. The final Vs tomography (Figs. S35–S37) revealed the high-V Pacific slab and prominent low-V anomalies in the mantle wedge, which are confirmed by the corresponding RRT test (Figs. S39 and S40). The subducting PHS slab, however, is not revealed clearly by the Rayleigh-wave tomography (Fig. S37), mainly because the resolution of this tomography is not high enough to image the thin and warm PHS slab beneath SW Japan.

4.3. Joint inversion of body-wave and surface-wave data

We conducted joint inversions of the Rayleigh-wave phase-velocity data (Fig. 13) and the S-wave travel-time data of local earthquakes and teleseismic events. Many tomographic inversions are performed to find the optimal values of the damping, smoothing and iteration parameters. The optimal values of these parameters are shown in Table S1. The RMS residuals of the local and teleseismic S-wave data as well as the Rayleigh-wave phase-velocity data are all reduced significantly after the joint inversion (Fig. S7f–h). The lateral grid interval is 0.33° in the optimal tomographic model. The obtained Vs images (Figs. 14–16) are similar to those of the body-wave tomography (Figs. 9–11), but the images are much improved for the surrounding oceanic regions, thanks to the Rayleigh-wave data which sample the oceanic areas very well (Fig. S32). Obvious low-V anomalies are revealed beneath

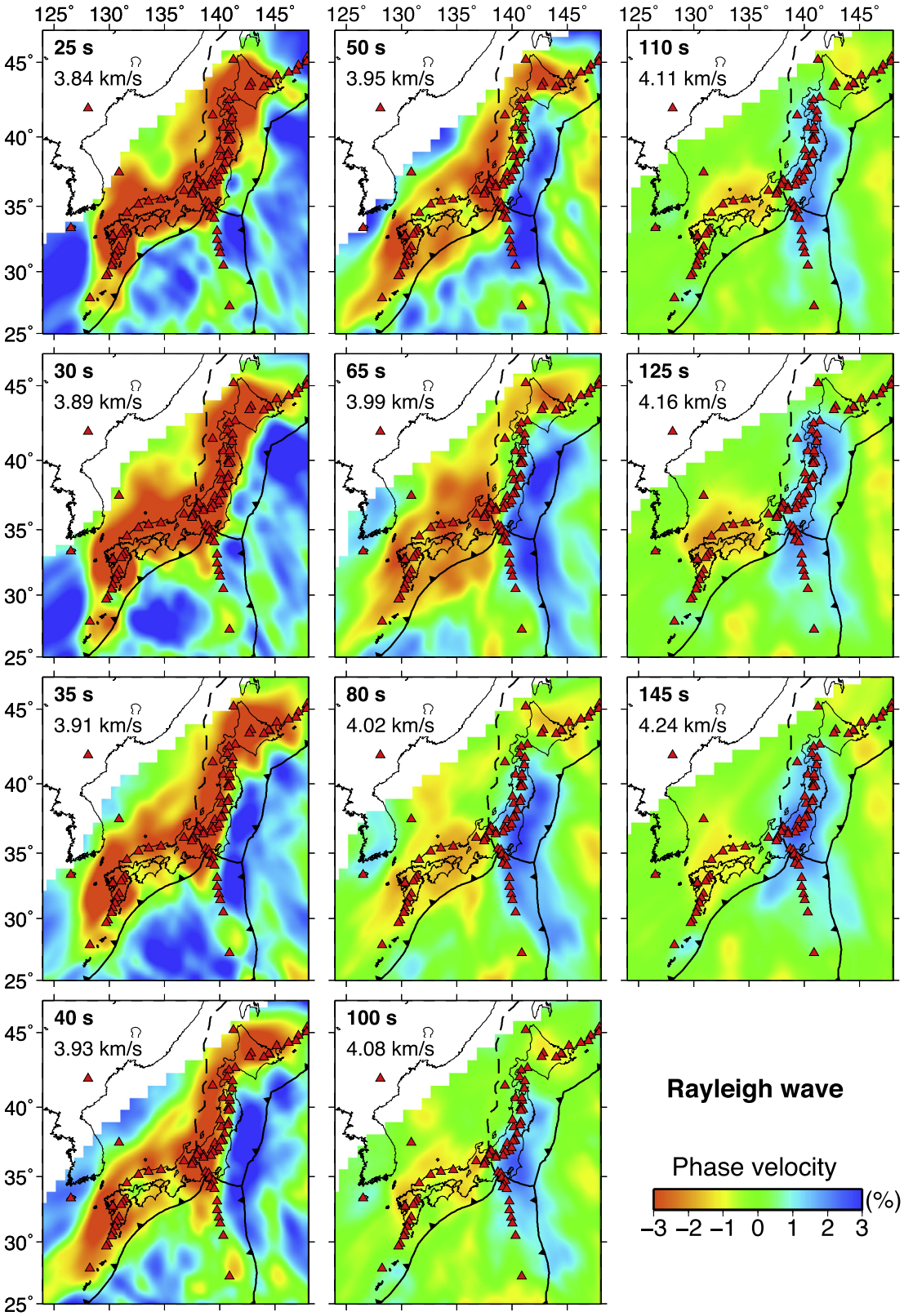

Fig. 13. Map views of Rayleigh-wave phase-velocity tomography at 11 different periods. The 1-D phase velocity at each period is shown in each map. The red and blue colors denote low and high phase velocities, respectively. The phase-velocity perturbation (in %) scale is shown at the bottom. The other labeling is the same as that in Fig. 6. (For interpretation of the references to color in this figure legend, the reader is referred to the web version of this article.)

the back-arc regions. The main features of the obtained Vs tomography (Figs. 14–16) are confirmed to be robust by the corresponding RRT test (Figs. S41 and S42).

To further confirm our tomographic results, we conducted a joint inversion of the local-earthquake S-wave arrival times and the Rayleigh-wave phase-velocity data. The RMS residuals of both

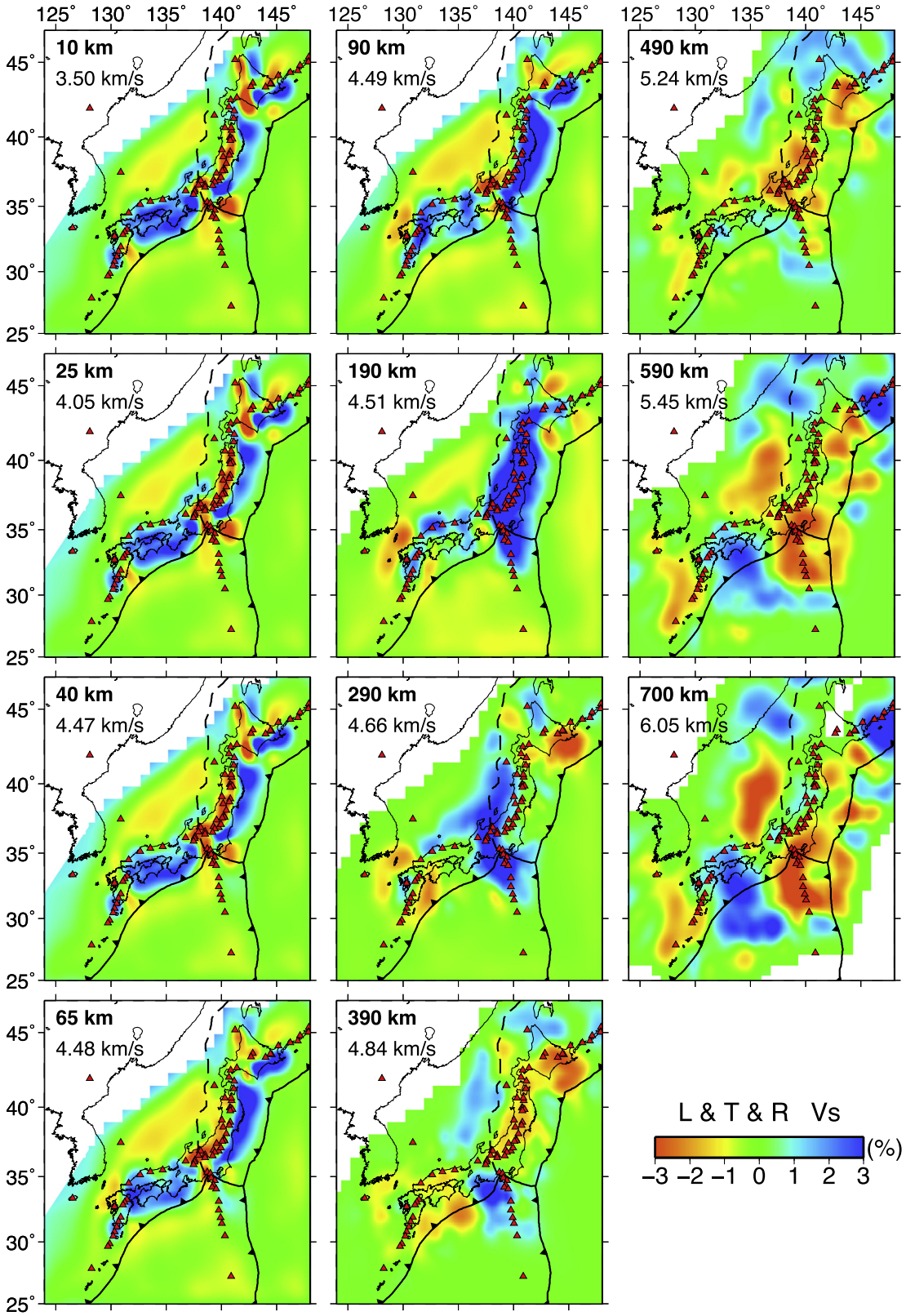

Fig. 14. Map views of Vs tomography determined by a joint inversion of the local and teleseismic S-wave travel-time data and the Rayleigh-wave phase-velocity data. The other labeling is the same as that in Fig. 6.

the local-earthquake S-wave data and the phase-velocity data are reduced significantly after the joint inversion (Fig. S43a,b). Figs. 17 and 18 and S44-S46 show the obtained 3-D Vs model, which is confirmed to be reliable by the corresponding synthetic test (Figs. S47 and S48). Although the main pattern of this Vs model (Figs. S44–S46) is similar to that of the tomography resulting from the local-earthquake S-wave data alone (Figs. S21–S23), the images are much improved for the back-arc areas (Figs. 17 and 18).

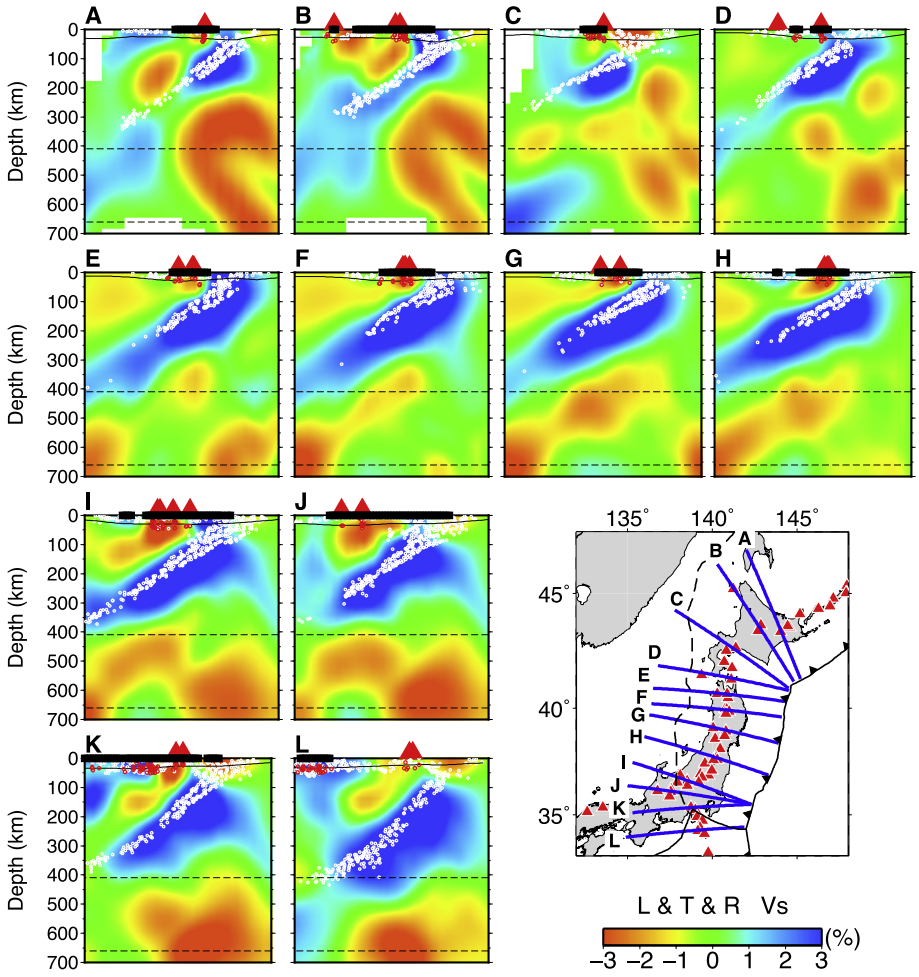

Fig. 15. Vertical cross-sections of Vs tomography along the profiles (blue lines) shown on the inset map, which are obtained by a joint inversion of the local and teleseismic S-wave travel-time data and the Rayleigh-wave phase-velocity data. The other labeling is the same as that in Fig. 7. (For interpretation of the references to color in this figure legend, the reader is referred to the web version of this article.)

We also conducted a joint inversion of the teleseismic S-wave residuals and the Rayleigh-wave phase-velocity data. The RMS residuals of both the teleseismic S-wave data and the phase-velocity data are reduced significantly after the joint inversion (Fig. S43c,d). The obtained 3-D Vs model is shown in Figs. 17, 18 and S49–S51. As compared with the tomography obtained with the teleseismic S-wave data alone (Figs. S29–S31), the joint-inversion results better constrain the shallow velocity structure (Figs. S49–S51). The corresponding synthetic test (Figs. S52 and S53) has confirmed the inversion results.

Figs. 17 and 18 show comparisons of the seven Vs models obtained by inverting each of the three data sets (i.e., the local-earthquake S-wave arrivals, the teleseismic S-wave residuals, and the Rayleigh-wave phase-velocity data) and their joint inversions. These Vs models are confirmed by the corresponding RRT results (Figs. S54 and S55). The main patterns of these models are generally similar to each other. The local body-wave data and the surface-wave data can constrain the shallow structure well down to ~300 km depth, whereas the teleseismic body-wave data mainly constrain the deeper structure of the study region. The surface-wave data can reveal the structural features beneath the surrounding oceanic regions. Although the surface-wave data at periods of 20–150 s have wavelengths of ~70–650 km which are much longer than those of the body-wave data, especially for the high-frequency local data, our results (Figs. 17 and 18) show that the smearing effect in the joint inversion is not obvious. A joint inversion of the different kinds of seismic data has resulted in a much more robust 3-D Vs model of the Japan subduction zone (Figs. 17 and 18).

With the 3-D Vs model obtained by the joint inversion of the local and teleseismic S-wave travel-time data and the Rayleigh-wave phase-velocity data, we also determined Poisson's ratio images of the study region. The obtained results (Figs. S56–S58) are similar to those shown in Figs. S12–S14, but the images are much improved in the surrounding oceanic regions, thanks to the Rayleigh-wave data which sample the oceanic areas very well (Fig. S32).

Our present tomographic results are compared with a regional Vp tomography (Wei et al., 2012) (Fig. 19). This 3-D Vp model has a spatial resolution of ~100 km in and around the Japan Islands. The main features of these different velocity models are generally similar to each other. However, our present results have a much better spatial resolution in and around Japan, thanks to the use of abundant high-quality body-wave and surface-wave data which were recorded by the dense seismic networks in the study region.

5. Discussion

5.1. Subducting oceanic slabs

Our results (Figs. 6–19) show that the subducting Pacific slab is imaged clearly as a dipping high-V zone beneath NE Japan,

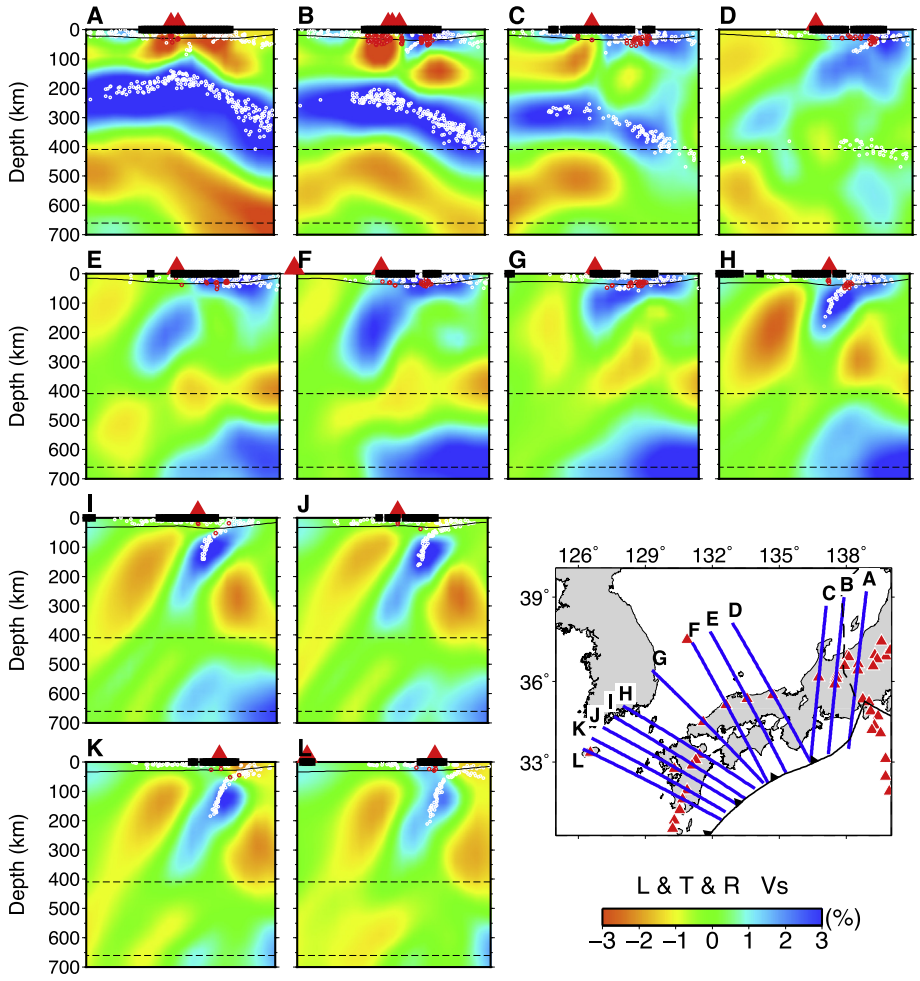

Fig. 16. The same as Fig. 15 but for vertical cross-sections beneath SW Japan.

whereas it becomes stagnant in the mantle transition zone (MTZ) beneath SW Japan. These features are confirmed by our detailed resolution tests (Figs. S8–S11 and S41–S42), and they are consistent with the previous large-scale regional and global tomographic results (e.g. Friederich (2003), Gorbatov and Kennett (2003), Huang and Zhao (2006), Koulakov (2011), Wei et al. (2012, 2015), Chen et al. (2015b), Obayashi et al. (2013), Zhao et al. (2013)). Recent P- and S-wave attenuation (Q) tomography beneath NE Japan revealed the subducting Pacific slab as a dipping high-Q zone (Liu et al., 2014), being consistent with the velocity tomography.

In most of the previous tomographic studies focusing on the deep structure of the Japan subduction zone (e.g. Zhao et al. (1994, 2012), Abdelwahed and Zhao (2007), Asamori and Zhao (2015)), the subducting Pacific slab with a thickness of 85–100 km was introduced into the starting model, because the upper boundary of the subducting Pacific slab is a sharp velocity discontinuity and its geometry has been determined reliably (e.g. Zhao et al. (1992, 2012)). These previous tomographic studies have shown that this approach can lead to a more reliable 3-D velocity model of the Japan subduction zone, because the slab could not be imaged very clearly if a simple 1-D starting model is adopted. However, the thickness of the Pacific slab was not well constrained by the previous tomographic results, because the rays then available did not crisscross very well near the lower boundary of the Pacific slab. In this study, we newly measured a great number of teleseismic data, and so the ray path coverage near the lower boundary of the Pacific slab is greatly improved, which enables us to constrain the thickness of the Pacific slab. Although a 1-D starting model is adopted for the tomographic inversion, our results (Figs. 6–19) have revealed the Pacific slab of ~100 km thick with its clear upper and lower boundaries, which is a reliable feature because our tomographic model has a spatial resolution of ~30 km in the horizontal direction and ~25 km in depth. Our results also show that the stagnant Pacific slab in the MTZ beneath SW Japan becomes slightly thicker. However, the resolution of our 3-D velocity models becomes lower in the MTZ, which should be improved in future studies.

The subducting PHS slab has a complex geometry (e.g., Figs. 1, 8 and 16). Our results (Figs. 6–19) have revealed the PHS slab clearly as a dipping high-V zone, which is confirmed by our detailed resolution tests (Figs. S8–S11 and S41–S42). Many non-volcanic low-frequency micro-earthquakes occurred along the upper boundary of the PHS slab beneath the forearc region in SW Japan (e.g., Figs. 8 and 16). Recent P- and S-wave attenuation tomography has revealed the PHS slab as a dipping high-Q zone (Liu and Zhao, 2014, 2015). Previous studies of local and teleseismic joint inversion have revealed that the PHS slab has subducted aseismically down to the MTZ depth under SW Japan, though the seismicity within the PHS slab ends at ~180 km depth, and a window (hole) exists within the aseismic PHS slab (Zhao et al., 2012; Huang et al., 2013; Asamori and Zhao, 2015). In this study, we newly measured a large number of teleseismic data, which greatly improve the ray path coverage in and around the PHS slab. Our results show that parts of the PHS slab have reached ~400 km depth beneath the Japan Sea and the East China Sea (e.g., Figs. 8 and 16), supporting the previous results.

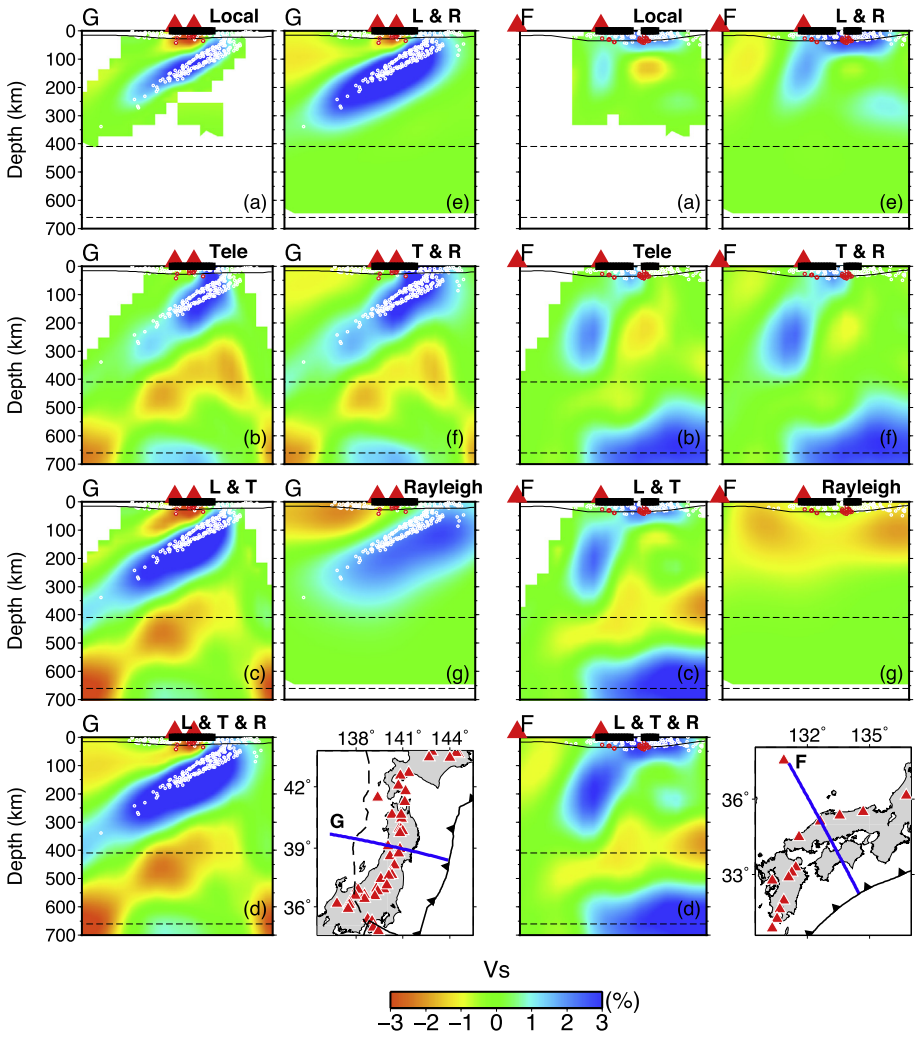

Fig. 17. Vertical cross-sections of Vs tomography along two profiles (blue lines) shown on the inset maps. The images are obtained by inverting (a) the local-earthquake S-wave arrival times, (b) teleseismic S-wave relative residuals, (g) Rayleigh-wave phase-velocity data, (c) joint inversion of local and teleseismic S-wave data which are also shown in Figs. 10 and 11, (d) joint inversion of the Rayleigh-wave phase-velocity data and the local and teleseismic S-wave data, (e) joint inversion of the Rayleigh-wave phase-velocity data and local-earthquake S-wave data, and (f) joint inversion of the Rayleigh-wave phase-velocity data and teleseismic S-wave data. The labeling is the same as that in Fig. 7. (For interpretation of the references to color in this figure legend, the reader is referred to the web version of this article.)

5.2. Hot mantle upwelling

Besides the significant high-V zones representing the subducting Pacific and PHS slabs, prominent low-V anomalies are revealed in the mantle wedge above the slabs and in the mantle below the slabs (Figs. 6–19). The results of synthetic tests (Figs. S8–S11 and S41–S42) indicate that these low-V zones are reliable features. The low-V anomalies imaged by this work are generally consistent with those revealed by previous studies (e.g. Zhao et al. (1992, 2012), Abdelwahed and Zhao (2007), Huang et al. (2015a), Wei et al. (2015), Asamori and Zhao (2015)), but the images are much improved for the back-arc areas and the mantle below the Pacific slab, thanks to the Rayleigh-wave data and abundant high-quality teleseismic data used in this study (Figs. 17 and 18). We think that the distinct velocity contrasts between the subducting slabs and the surrounding mantle reflect significant variations in temperature as well as water content and/or the degree of partial melting.

Low-V anomalies are clearly visible in the mantle wedge above the Pacific slab beneath NE and SW Japan (Figs. 6–19). In NE Japan, a sheet-like low-V zone exists in the mantle wedge beneath the volcanic front and extends to the back-arc side, which reflects the source zone of arc magmatism and corner flow in the mantle wedge (Zhao et al., 1992, 2012). Many low-frequency micro-earthquakes occurred in or around the low-V zones in the lower crust and uppermost mantle (e.g., Figs. 7 and 15) probably due to the arc magma rising from the mantle wedge to the crust (Hasegawa et al., 2013; Zhao et al., 1992). In SW Japan, obvious low-V anomalies exist in the big mantle wedge above the Pacific slab and below the PHS slab, which reflects hot and wet upwelling from the deep portion of the mantle wedge and deep dehydration of the stagnant Pacific slab in the MTZ (Zhao et al., 2012). This mantle upwelling may distort the PHS slab and cause its complex geometry and the slab window (Asamori and Zhao, 2015). Recent P- and S-wave attenuation tomography has revealed obvious low-Q zones in the mantle wedge above the Pacific slab (Liu et al., 2014; Liu and Zhao, 2014, 2015). The mantle-wedge low-Q zones generally coincide with the low-V anomalies obtained by this study.

Prominent low-V anomalies are also visible in the mantle wedge above the PHS slab beneath SW Japan (e.g., Figs. 8 and 16), which are generally consistent with those revealed by the previous studies (e.g. Abdelwahed and Zhao (2007), Xia et al. (2008), Zhao et al. (2012), Liu et al. (2013b), Huang et al. (2013), Asamori and Zhao (2015)), but the images are much improved for the back-arc areas, due to the addition of Rayleigh-wave phase-

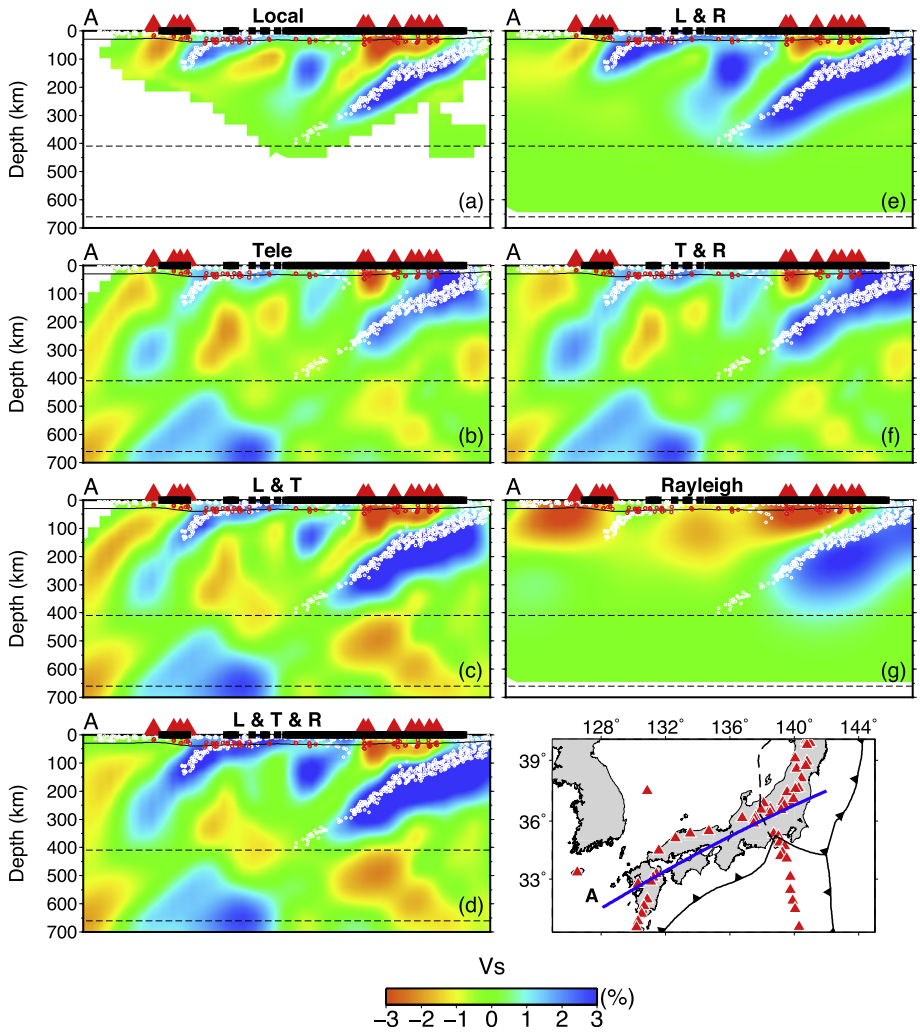

Fig. 18. The same as Fig. 17 but for Vs tomography along a different profile shown on the inset map.

velocity data used in this work (Figs. 17 and 18). Many low-frequency micro-earthquakes also occurred in or around the low-V anomalies in the lower crust and uppermost mantle beneath the arc volcanoes in SW Japan (e.g., Figs. 8 and 16). These low-V anomalies also coincide with the low-Q zones in the mantle wedge above the PHS slab revealed by attenuation tomography (Liu and Zhao, 2014, 2015). Such low-V and low-Q anomalies in the mantle wedge have been also revealed in many other subduction zones, such as Tonga (Zhao et al., 1997b; Roth et al., 1999, 2000), Alaska (Stachnik et al., 2004; Qi et al., 2007; Tian and Zhao, 2012), Kamchatka (Jiang et al., 2009), New Zealand (Eberhart-Phillips and Bannister, 2015), Mariana (Pozgay et al., 2009; Barklage et al., 2015), Cascadia (e.g. Chen et al. (2015a)) and Indonesia (e.g. Huang et al. (2015b)). Such a feature is a common seismological characteristic of subduction zones, which reflects the source of arc magmatism caused by a combination of slab dehydration and corner flow in the mantle wedge (Zhao et al., 1992, 2012; Iwamori and Zhao, 2000; Wiens et al., 2008).

Our tomography also shows significant low-V anomalies in the mantle below the Pacific slab (e.g., Figs. 7 and 15), which are confirmed by our detailed resolution analyses (Figs. S8 and S41). Such a feature has been also revealed by the large-scale regional and global tomography (e.g. Zhao (2004), Huang and Zhao (2006), Wei et al. (2012, 2015)), as well as by the previous studies of local and teleseismic joint inversion (Zhao et al., 1994, 2012; Abdelwahed and Zhao, 2007; Asamori and Zhao, 2015). Global tomography suggests that the sub-slab low-V anomalies originate from the lower mantle at a depth of ~1500 km (Zhao, 2004; Zhao et al., 2013). Recent regional tomography shows that the low-V anomalies are visible down to at least ~1100 km depth (Wei et al., 2015). These low-V anomalies may reflect hot mantle upwelling as a consequence of thermal instability associated with collapsing of the stagnant Pacific slab materials from the MTZ down to the lower mantle as a result of very large gravitational instability from phase transitions (Maruyama et al., 2007; Zhao et al., 2012). In this work, we have imaged the sub-slab low-V anomalies more clearly than the previous works. In some vertical cross-sections beneath NE Japan (e.g., Figs. 7 and 15), the sub-slab low-V anomalies exhibit a sheet-like zone sub-parallel to the Pacific slab at depths of ~150–700 km. This sheet-like low-V zone may reflect a subducting asthenosphere underlying the Pacific slab. The boundary between the Pacific slab and the underlying asthenosphere seems to be clear beneath NE Japan (e.g., Figs. 7 and 15). Morgan et al. (2013) proposed that a plume-fed asthenosphere might exist beneath the Pacific plate. We think that parts of the possible plume-fed asthenosphere may be subducting beneath NE Japan together with the Pacific slab. In addition, such a subducting asthenosphere may be also affected by hot mantle upwelling from the deeper mantle as revealed by global tomography (e.g. Zhao (2004), Obayashi et al. (2013), Zhao et al. (2013)). Future detailed

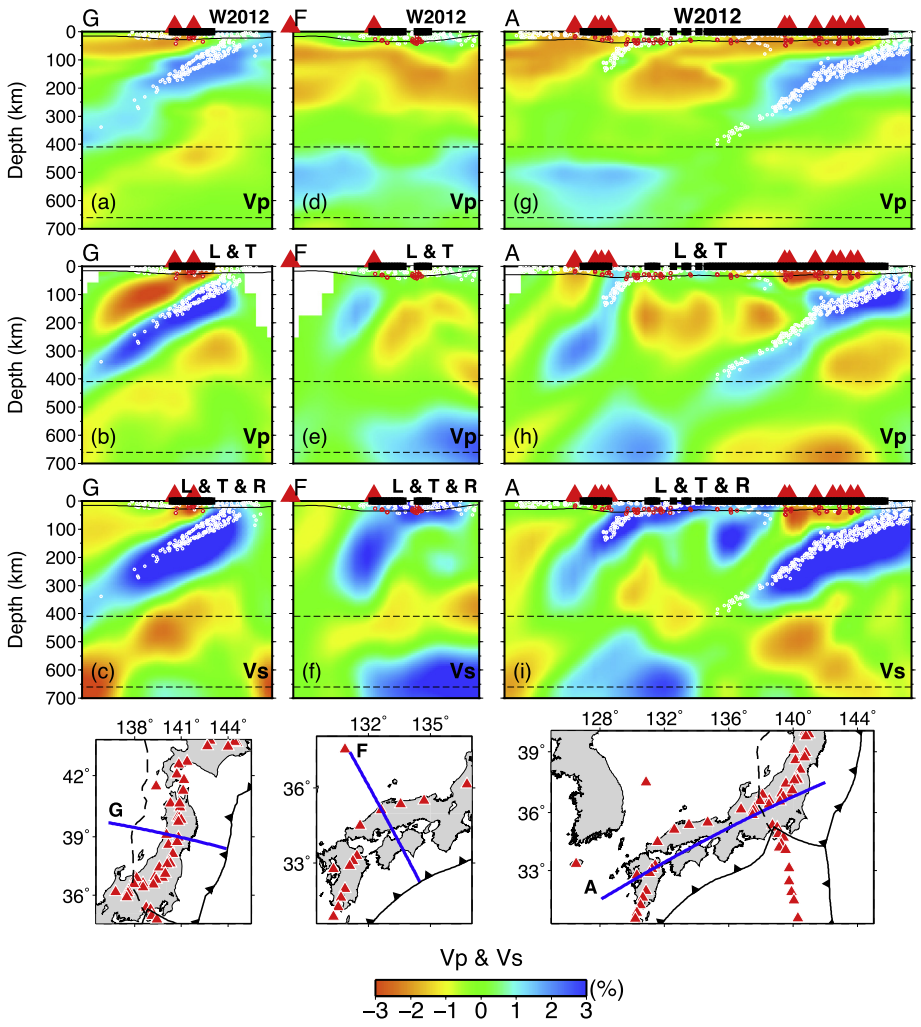

Fig. 19. Vertical cross-sections of Vp and Vs tomography along three profiles (blue lines) shown on the inset maps. The Vp images (W2012) shown in (a, d, g) are from the regional tomography model of Wei et al. (2012). The Vp images shown in (b, e, h) are obtained by our joint inversion of the P-wave travel-time data of local earthquakes and teleseismic events. The Vs images shown in (c, f, i) are obtained by our joint inversion of the Rayleigh wave phase-velocity data and the local and teleseismic travel-time data. The labeling is the same as that in Figs. 17 and 18. (For interpretation of the references to color in this figure legend, the reader is referred to the web version of this article.)

studies of anisotropic tomography for the Pacific slab and the underlying asthenosphere may shed new light on the structure and dynamics in the deep part of subduction zones (e.g. Tian and Zhao (2012), Wang and Zhao (2012, 2013), Huang et al. (2015b), Wei et al. (2015), Zhao et al. (2016)).

6. Conclusions

We measured over half a million high-quality P- and S-wave arrival-time data from over 700 teleseismic events recorded during the past 10 years by the dense seismic network on the Japan Islands. Joint inversions of the travel-time data from local earthquakes and teleseismic events are conducted to determine detailed Vp and Vs tomography of the crust and mantle down to 700 km depth beneath the Japan Islands. We also determined 2-D Rayleigh-wave phase-velocity distributions at periods of 20–150 s beneath Japan using the teleseismic fundamental mode Rayleigh-wave amplitude and phase data. Joint inversions of the local and teleseismic S-wave travel times and Rayleigh-wave phase-velocity data are performed to determine a detailed Vs tomography of the Japan subduction zone. The obtained results are similar to those of the body-wave tomography, but the images of the surrounding oceanic regions are much improved, thanks to the surface-wave data which sample the oceanic areas very well.

Our present tomography revealed clearly the subducting Pacific and Philippine Sea slabs and prominent low-V anomalies in the surrounding mantle beneath the Japan Islands. The distinct structures of the subducting slabs and the surrounding mantle reflect their significant differences in temperature and other properties such as water content and/or the degree of partial melting. The reliability and robustness of the present results indicate that joint inversions of different kinds of seismic data are very effective and important for improving our understanding of the structure and dynamics of subduction zones.

Acknowledgments

We thank the data centers of the Japanese seismic networks and the JMA Unified Earthquake Catalog for providing the high-quality waveform and arrival-time data used in this study. Some of the arrival-time data were measured from the original seismograms by the staffs of Research Center for Prediction of Earthquakes and Volcanic Eruptions, Tohoku University. We also thank Dr. Wei Wei for sharing their Vp tomographic model. The free software GMT (Wessel and Smith, 1998), SAC (Goldstein et al., 2003), and TauP (Crotwell et al., 1999) are used. The discussions with Drs. W. Wei, Z. Huang, G. Jiang and S. Xia were very helpful. We appreciate the thoughtful review comments and suggestions from

Prof. V. Cormier (the Editor) and two anonymous reviewers. This work was partially supported by Grants from the JSPS (Kiban-S 23224012) and the MEXT (26106005) to D. Zhao.

Appendix A. Supplementary data

Supplementary data associated with this article can be found, in the online version, at http://dx.doi.org/10.1016/j.pepi.2016.01.002.

References

Abdelwahed, M., Zhao, D., 2007. Deep structure of the Japan subduction zone. Phys. Earth Planet. Inter. 162, 32–52.

Asamori, K., Zhao, D., 2015. Teleseismic shear wave tomography of the Japan subduction zone. Geophys. J. Int. 203, 1752–1772.

Barklage, M., Wiens, D., Conder, J., Pozgay, S., Shiobara, H., Sugioka, H., 2015. P and S velocity tomography of the Mariana subduction system from a combined land-sea seismic deployment. Geochem. Geophys. Geosyst. 16, 681–704.

Chen, C., Zhao, D., Wu, S., 2015a. Tomographic imaging of the Cascadia subduction zone: constraints on the Juan de Fuca slab. Tectonophysics 647, 73–88.

Chen, M., Niu, F., Liu, Q., Tromp, J., Zheng, X., 2015b. Multiparameter adjoint tomography of the crust and upper mantle beneath East Asia: 1. Model construction and comparisons. J. Geophys. Res. 120, 1762–1786.

Crotwell, H., Owens, T., Ritsema, J., 1999. The TauP toolkit: flexible seismic travel-time and ray-path utilities. Seismol. Res. Lett. 70, 154–160.

Dahlen, F., Hung, S., Nolet, G., 2000. Fréchet kernels for finite-frequency traveltimes—I. Theory. Geophys. J. Int. 141, 157–174.

Dziewonski, A., Anderson, D., 1981. Preliminary reference Earth model. Phys. Earth Planet. Inter. 25, 297–356.

Eberhart-Phillips, D., Bannister, S., 2015. 3-D imaging of the northern Hikurangi subduction zone, New Zealand: variations in subducted sediment, slab fluids and slow slip. Geophys. J. Int. 201, 838–855.

Forsyth, D., Li, A., 2005. Array analysis of two-dimensional variations in surface wave phase velocity and azimuthal anisotropy in the presence of multipathing interference. In: Levander, A., Nolet, G. (Ed.), Seismic Earth: Array Analysis of Broadband Seismograms, Geophysical Monograph, vol. 157, AGU, Washington, D.C, pp. 81–97.

Friederich, W., 2003. The S-velocity structure of the East Asian mantle from inversion of shear and surface waveforms. Geophys. J. Int. 153, 88–102.

Goldstein, P., Dodge, D., Firpo, M., Minner, L., 2003. SAC2000: signal processing and analysis tools for seismologists and engineers. In: Lee, W. et al. (Eds.), The IASPEI International Handbook of Earthquake and Engineering Seismology. Academic Press, London, U. K., pp. 1613–1641.

Gorbatov, A., Kennett, B., 2003. Joint bulk-sound and shear tomography for Western Pacific subduction zones. Earth Planet. Sci. Lett. 210, 527–543.

Hasegawa, A., Nakajima, J., Yanada, T., Uchida, N., Okada, T., Zhao, D., Matsuzawa, T., Umino, N., 2013. Complex slab structure and arc magmatism beneath the Japanese Islands. J. Asian Earth Sci. 78, 277–290.

Huang, J., Zhao, D., 2006. High-resolution mantle tomography of China and surrounding regions. J. Geophys. Res. 111, B09305. http://dx.doi.org/10.1029/2005JB004066.

Huang, Z., Zhao, D., Hasegawa, A., Umino, N., Park, J., Kang, I., 2013. Aseismic deep subduction of the Philippine Sea plate and slab window. J. Asian Earth Sci. 75, 82–94.

Huang, Z., Zhao, D., Liu, X., 2015a. On the trade-off between seismic anisotropy and heterogeneity: numerical simulations and application to Northeast Japan. J. Geophys. Res. 120, 3255–3277.

Huang, Z., Zhao, D., Wang, L., 2015b. P-wave tomography and anisotropy beneath Southeast Asia: insight into mantle dynamics. J. Geophys. Res. 120, 5154–5174.

Hung, S., Dahlen, F., Nolet, G., 2000. Fréchet kernels for finite-frequency traveltimes—II. Examples. Geophys. J. Int. 141, 175–203.

Iwamori, H., Zhao, D., 2000. Melting and seismic structure beneath the northeast Japan arc. Geophys. Res. Lett. 27, 425–428.

Jiang, G., Zhao, D., Zhang, G., 2009. Seismic tomography of the Pacific slab edge under Kamchatka. Tectonophysics 465, 190–203.

Kennett, B., Engdahl, E., 1991. Traveltimes for global earthquake location and phase identification. Geophys. J. Int. 105, 429–465.

Koulakov, I., 2011. High-frequency P and S velocity anomalies in the upper mantle beneath Asia from inversion of worldwide traveltime data. J. Geophys. Res. 116, B04301. http://dx.doi.org/10.1029/2010JB007938.

Laske, G., Masters, G., Ma, Z., Pasyanos, M., 2013. Update on CRUST1.0 – A 1-degree Global Model of Earth's Crust. Geophysical Research Abstracts 15, Abstract EGU2013-2658.

Lees, J., VanDecar, J., 1991. Seismic tomography constrained by Bouguer gravity anomalies: applications in western Washington. Pure Appl. Geophys. 135, 31–52.

Liu, X., Zhao, D., Li, S., 2013a. Seismic heterogeneity and anisotropy of the southern Kuril arc: insight into megathrust earthquakes. Geophys. J. Int. 194, 1069–1090.

Liu, X., Zhao, D., Li, S., 2013b. Seismic imaging of the Southwest Japan arc from the Nankai trough to the Japan Sea. Phys. Earth Planet. Inter. 216, 59–73.

Liu, X., Zhao, D., Li, S., 2014. Seismic attenuation tomography of the Northeast Japan arc: insight into the 2011 Tohoku earthquake (Mw 9.0) and subduction dynamics. J. Geophys. Res. 119, 1094–1118.

Liu, X., Zhao, D., 2014. Structural control on the nucleation of megathrust earthquakes in the Nankai subduction zone. Geophys. Res. Lett. 41, 8288–8293.

Liu, X., Zhao, D., 2015. Seismic attenuation tomography of the Southwest Japan arc: new insight into subduction dynamics. Geophys. J. Int. 201, 135–156.

Maruyama, S., Santosh, M., Zhao, D., 2007. Superplume, supercontinent, and post-perovskite: mantle dynamics and anti-plate tectonics on the core-mantle boundary. Gondwana Res. 11, 7–37.

Morgan, J., Hasenclever, J., Shi, C., 2013. New observational and experimental evidence for a plume-fed asthenosphere boundary layer in mantle convection. Earth Planet. Sci. Lett. 366, 99–111.

Nakajima, J., Hirose, F., Hasegawa, A., 2009. Seismotectonics beneath the Tokyo metropolitan area, Japan: effect of slab-slab contact and overlap on seismicity. J. Geophys. Res. 114, B08309. http://dx.doi.org/10.1029/2008JB006101.

Obayashi, M., Yoshimitsu, J., Nolet, G., Fukao, Y., Shiobara, H., Sugioka, H., Miyamachi, H., Gao, Y., 2013. Finite frequency whole mantle P wave tomography: improvement of subducted slab images. Geophys. Res. Lett. 40, 5652–5657.

Okada, Y., Kasahara, K., Hori, S., Obara, K., Sekiguchi, S., Fujiwara, H., Yamamoto, A., 2004. Recent progress of seismic observation networks in Japan: Hi-net, F-net, K-net and KiK-net. Earth Planets Space 56, 15–28.

Paige, C., Saunders, M., 1982. LSQR: an algorithm for sparse linear equations and sparse least squares. ACM Trans. Math. Software 8, 43–71.

Press, W., Teukolsky, S., Vetterling, W., Flannery, B., 1992. Numerical Recipes in FORTAN: The Art of Scientific Computing, second ed. Cambridge University Press, Cambridge.

Pozgay, S., Wiens, D., Conder, J., Shiobara, H., Sugioka, H., 2009. Seismic attenuation tomography of the Mariana subduction system: implications for thermal structure, volatile distribution, and slow spreading dynamics. Geochem. Geophys. Geosyst. 10, Q04X05. http://dx.doi.org/10.1029/2008GC002313.

Qi, C., Zhao, D., Chen, Y., 2007. Search for deep slab segments under Alaska. Phys. Earth Planet. Inter. 165, 68–82.

Roth, E., Wiens, D., Dorman, L., Hildebrand, J., Webb, S., 1999. Seismic attenuation tomography of the Tonga-Fiji region using phase pair methods. J. Geophys. Res. 104, 4795–4809.

Roth, E., Wiens, D., Zhao, D., 2000. An empirical relationship between seismic attenuation and velocity anomalies in the upper mantle. Geophys. Res. Lett. 27, 601–604.

Saito, M., 1988. DISPER80: a subroutine package for the calculation of seismic normal mode solutions. In: Doornbos, D. (Ed.), Seismological Algorithms: Computational Methods and Computer Programs. Academic Press, New York, pp. 293–319.

Stachnik, J., Abers, G., Christensen, D., 2004. Seismic attenuation and mantle wedge temperatures in the Alaska subduction zone. J. Geophys. Res. 109, B10304. http://dx.doi.org/10.1029/2004JB003018.

Syracuse, E., Maceira, M., Zhang, H., Thurber, C., 2015. Seismicity and structure of Akutan and Makushin Volcanoes, Alaska, using joint body and surface wave tomography. J. Geophys. Res. 120, 1036–1052.

Tian, Y., Zhao, D., 2012. Seismic anisotropy and heterogeneity in the Alaska subduction zone. Geophys. J. Int. 190, 629–649.

Tong, P., Zhao, D., Yang, D., 2011. Tomography of the 1995 Kobe earthquake area: comparison of finite-frequency and ray approaches. Geophys. J. Int. 187, 278–302.

Tong, P., Zhao, D., Yang, D., 2012. Tomography of the 2011 Iwaki earthquake (M 7.0) and Fukushima nuclear power plant area. Solid Earth 3, 43–51.

VanDecar, J., Crosson, R., 1990. Determination of teleseismic relative phase arrival times using multi-channel cross-correlation and least squares. Bull. Seismol. Soc. Am. 80, 150–169.

Villagómez, D., Toomey, D., Geist, D., Hooft, E., Solomon, S., 2014. Mantle flow and multistage melting beneath the Galapagos hotspot revealed by seismic imaging. Nat. Geosci. 7, 151–156.

Wang, J., Zhao, D., 2012. P-wave anisotropic tomography of the Nankai subduction zone in Southwest Japan. Geochem. Geophys. Geosyst. 13, Q05017. http://dx.doi.org/10.1029/2012GC004081.

Wang, J., Zhao, D., 2013. P-wave tomography for 3-D radial and azimuthal anisotropy of Tohoku and Kyushu subduction zones. Geophys. J. Int. 193, 1166–1181.

Wei, W., Xu, J., Zhao, D., Shi, Y., 2012. East Asia mantle tomography: New insight into plate subduction and intraplate volcanism. J. Asian Earth Sci. 60, 88–103.

Wei, W., Zhao, D., Xu, J., Wei, F., Liu, G., 2015. P and S wave tomography and anisotropy in Northwest Pacific and East Asia: constraints on stagnant slab and intraplate volcanism. J. Geophys. Res. 120, 1642–1666.

Wessel, P., Smith, W., 1998. New, improved version of the generic mapping tools released. EOS Trans. Am. Geophys. Union 79, 579.

Wiens, D., Conder, J., Faul, U., 2008. The seismic structure and dynamics of the mantle wedge. Annu. Rev. Earth Planet. Sci. 36, 421–455.

Xia, S., Zhao, D., Qiu, X., 2008. Tomographic evidence for the subducting oceanic crust and forearc mantle serpentinization under Kyushu, Japan. Tectonophysics 449, 85–96.

Yang, Y., Forsyth, D., 2006. Regional tomographic inversion of the amplitude and phase of Rayleigh waves with 2-D sensitivity kernels. Geophys. J. Int. 166, 1148–1160.

Yoshizawa, K., Miyake, K., Yomogida, K., 2010. 3D upper mantle structure beneath Japan and its surrounding region from inter-station dispersion measurements of surface waves. Phys. Earth Planet. Inter. 183, 4–19.
Zhang, H., Maceira, M., Roux, P., Thurber, C., 2014. Joint inversion of body-wave arrival times and surface-wave dispersion for three-dimensional seismic structure around SAFOD. Pure Appl. Geophys. 171, 3013–3022.
Zhang, Y., Tanimoto, T., 1993. High-resolution global upper mantle structure and plate tectonics. J. Geophys. Res. 98, 9793–9823.
Zhao, D., Hasegawa, A., Horiuchi, S., 1992. Tomographic imaging of P and S wave velocity structure beneath northeastern Japan. J. Geophys. Res. 97, 19909–19928.
Zhao, D., Hasegawa, A., Kanamori, H., 1994. Deep structure of Japan subduction zone as derived from local, regional, and teleseismic events. J. Geophys. Res. 99, 22313–22329.
Zhao, D., Kanamori, H., Negishi, H., Wiens, D., 1996. Tomography of the source area of the 1995 Kobe earthquake: evidence for fluids at the hypocenter? Science 274, 1891–1894.
Zhao, D., Matsuzawa, T., Hasegawa, A., 1997a. Morphology of the subducting slab boundary in the northeastern Japan arc. Phys. Earth Planet. Inter. 102, 89–104.
Zhao, D., Xu, Y., Wiens, D., Dorman, L., Hildebrand, J., Webb, S., 1997b. Depth extent of the Lau back-arc spreading center and its relation to subduction processes. Science 278, 254–257.
Zhao, D., 2004. Global tomographic images of mantle plumes and subducting slabs: insight into deep Earth dynamics. Phys. Earth Planet. Inter. 146, 3–34.
Zhao, D., Yanada, T., Hasegawa, A., Umino, N., Wei, W., 2012. Imaging the subducting slabs and mantle upwelling under the Japan Islands. Geophys. J. Int. 190, 816–828.
Zhao, D., Yamamoto, Y., Yanada, T., 2013. Global mantle heterogeneity and its influence on teleseismic regional tomography. Gondwana Res. 23, 595–616.
Zhao, D., 2015. The 2011 Tohoku earthquake (Mw 9.0) sequence and subduction dynamics in Western Pacific and East Asia. J. Asian Earth Sci. 98, 26–49.
Zhao, D., Yu, S., Liu, X., 2016. Seismic anisotropy tomography: new insight into subduction dynamics. Gondwana Res. http://dx.doi.org/10.1016/j.gr.2015.05.008.